The Astrophysical Journal, 827:20 (19pp), 2016 August 10 doi:10.3847/0004-637X/827/1/20

BREAKING THE CURVE WITH CANDELS: A BAYESIAN APPROACH TO REVEAL THE NON-UNIVERSALITY OF THE DUST-ATTENUATION LAW AT HIGH REDSHIFT

Brett Salmon[1], Casey Papovich[1], James Long[2], S. P. Willner[3], Steven L. Finkelstein[4], Henry C. Ferguson[5], Mark Dickinson[6], Kenneth Duncan[7,8], S. M. Faber[9], Nimish Hathi[10], Anton Koekemoer[5], Peter Kurczynski[11], Jeffery Newman[12], Camilla Pacifici[13], Pablo G. Pérez-González[14], and Janine Pforr[10]
[1] George P. and Cynthia W. Mitchell Institute for Fundamental Physics and Astronomy, Department of Physics and Astronomy, Texas A&M University, College Station, TX 77843, USA; bsalmon@physics.tamu.edu
[2] Department of Statistics, Texas A&M University, College Station, TX 77843-3143, USA
[3] Harvard-Smithsonian Center for Astrophysics, Cambridge, MA 02138, USA
[4] Department of Astronomy, The University of Texas at Austin, Austin, TX 78712, USA
[5] Space Telescope Science Institute, Baltimore, MD, USA
[6] National Optical Astronomy Observatories, Tucson, AZ, USA
[7] University of Nottingham, School of Physics & Astronomy, Nottingham NG7 2RD, UK
[8] Leiden Observatory, Leiden University, NL-2300 RA Leiden, The Netherlands
[9] UCO/Lick Observatory, Department of Astronomy and Astrophysics, University of California, Santa Cruz, CA 95064, USA
[10] Aix Marseille Université, CNRS, LAM (Laboratoire d'Astrophysique de Marseille) UMR 7326, F-13388, Marseille, France
[11] Department of Physics and Astronomy, Rutgers, The State University of New Jersey, Piscataway, NJ 08854, USA
[12] Department of Physics and Astronomy, University of Pittsburgh and PITT-PACC, 3941 O'Hara St., Pittsburgh, PA 15260, USA
[13] Astrophysics Science Division, Goddard Space Flight Center, Code 665, Greenbelt, MD 20771, USA
[14] Departamento de Astrofísica, Facultad de CC. Físicas,Universidad Complutense de Madrid, E-28040 Madrid, Spain
Received 2015 December 16; revised 2016 May 4; accepted 2016 May 25; published 2016 August 3

ABSTRACT

Dust attenuation affects nearly all observational aspects of galaxy evolution, yet very little is known about the form of the dust-attenuation law in the distant universe. Here, we model the spectral energy distributions of galaxies at $z \sim 1.5$–3 from CANDELS with rest-frame UV to near-IR imaging under different assumptions about the dust law, and compare the amount of inferred attenuated light with the observed infrared (IR) luminosities. Some individual galaxies show strong Bayesian evidence in preference of one dust law over another, and this preference agrees with their observed location on the plane of infrared excess (IRX, $L_{\rm TIR}/L_{\rm UV}$) and UV slope (β). We generalize the shape of the dust law with an empirical model, $A_{\lambda,\delta} = E(B-V)k_\lambda\,(\lambda/\lambda_V)^\delta$ where k_λ is the dust law of Calzetti et al., and show that there exists a correlation between the color excess $E(B-V)$ and tilt δ with $\delta = (0.62 \pm 0.05)\log(E(B-V)) + (0.26 \pm 0.02)$. Galaxies with high color excess have a shallower, starburst-like law, and those with low color excess have a steeper, SMC-like law. Surprisingly, the galaxies in our sample show no correlation between the shape of the dust law and stellar mass, star formation rate, or β. The change in the dust law with color excess is consistent with a model where attenuation is caused by scattering, a mixed star–dust geometry, and/or trends with stellar population age, metallicity, and dust grain size. This rest-frame UV-to-near-IR method shows potential to constrain the dust law at even higher redshifts ($z > 3$).

Key words: galaxies: evolution – galaxies: general – galaxies: high-redshift – galaxies: statistics

1. INTRODUCTION

Our knowledge of star formation rates (SFRs) among the majority of $z > 4$ galaxies is, except in rare cases, limited to observations in the rest-frame ultraviolet (UV) where the effects of the dust attenuation are most severe and lead to large systematics. Galaxy surveys at the highest redshifts are predominantly limited to studying the rest-frame UV-to-near-infrared (NIR) spectral energy distribution (SED). The dust attenuation at this critical portion of the SED cannot be dismissed even at $z = 7$–8, considering the mounting observations of high-redshift dusty star-forming galaxies, submillimeter galaxies, and quasars (Wang et al. 2008; Casey et al. 2014a; Mancuso et al. 2016). In addition, while there is no shortage of observations and simulations that offer potential mechanisms for dust production in the early universe (Todini & Ferrara 2001; Gall et al. 2011a, 2011b, 2011c; Ventura et al. 2014), it is still uncertain how, and to what degree, these mechanisms influence the wavelength dependence of attenuation at high redshift.

The nuances of dust geometry, extinction, and scattering from the interstellar medium and star-forming regions are often conveniently packaged into a "recipe" of reddening (Calzetti 1997), parameterized by a wavelength-dependent curve of the total-to-selective extinction (Witt & Gordon 2000, and references therein),

$$k_\lambda = A_\lambda/E(B-V) \text{ and } R_{\rm V} = A_{\rm V}/E(B-V), \quad (1)$$

where A_λ is the total extinction in magnitudes at wavelength λ and $E(B-V)$ is the color excess of selective extinction. We emphasize the distinction that dust "extinction" accounts for the absorption and scattering of light out of the line of sight, whereas "attenuation" also accounts for the spatial scattering of light into the line of sight for extended sources such as galaxies. We refer to both extinction and attenuation models as "dust laws" for brevity. Successful empirical and analytic dust laws have been used for decades as a necessary a priori assumption when inferring fundamental physical properties of distant galaxies (Meurer et al. 1999; Papovich et al. 2001).

Dust laws are already known to be non-universal across all galaxy types from derivations of the dust laws of the Small and Large Magellanic Clouds (SMC and LMC), and the Milky

Way, as well as dust attenuation in $z < 1$ galaxies (Conroy & Gunn 2010). For example, Kriek & Conroy (2013) have shown that the form of the dust law can vary significantly at $z < 2$ as a function of galaxy type, and in some cases it differs strongly from the conventionally assumed prescription of Calzetti et al. (2000), derived from local UV-luminous starbursts. The conditions that produce these unique dust laws are complex. They depend on the covering factor, the dust grain size (which is dependent on the observed composition and metallicity), and the line-of-sight geometry and can therefore change when galaxies are viewed at different orientations (Witt & Gordon 2000; Chevallard et al. 2013) or different ages of the stellar population (Charlot & Fall 2000).

Changes to the observed star–dust geometry, that is, the relative geometry between stars and dust grains, produce different dust laws even for galaxies of a similar type. For example, observations of the infrared excess (IRX $\equiv L_{\rm TIR}/L_{\rm UV}$) and the UV slope ($\beta$, where $f_\lambda \propto \lambda^\beta$ over $1268 < \lambda < 2580$ Å, Calzetti et al. 1994) have shown that star-forming galaxies bracket a range of attenuation types from starburst to SMC-like attenuations (Muñoz-Mateos et al. 2009; Buat et al. 2011, 2012; Overzier et al. 2011). The position of galaxies on the IRX–β plane suggests that a single dust-attenuation prescription is incapable of explaining all observations (Burgarella et al. 2005; Seibert et al. 2005; Papovich et al. 2006; Boquien et al. 2009; Casey et al. 2014b).

Although star-forming galaxies have a variety of attenuation scenarios, it is possible to infer their dust geometries by correlating their inferred dust laws with physical properties. For example, Reddy et al. (2015) studied a sample of $z \sim 2$ galaxies and found that the differences in attenuation between gas and stars are correlated with the galaxy's observed specific SFR (sSFR $\equiv$ SFR/$M_\star$), potentially a byproduct of the visibility of star-forming birth clouds. If the dust law is dependent on star formation activity, then it may be different at earlier epochs ($z > 2$). This follows intuition because the intensity of star formation and ionization conditions, which directly influence the attenuation conditions, have been shown to evolve with redshift (Casey et al. 2014b; Madau & Dickinson 2014; Steidel et al. 2014; Sanders et al. 2015; Shapley et al. 2015; Shimakawa et al. 2015). These attenuation conditions are regulated by the formation, destruction, and spatial distribution of dust grains, and this cycle is one of the most poorly quantified processes in galaxies. One reason to seek evidence for the dust law is to place constraints on the observed dust grain size, which can be used to infer limits on dust production by supernovae (SNe) and asymptotic giant branch (AGB) stars, especially given the maximum stellar population ages at the redshifts of distant galaxies.

While the dust law gives clues to the underlying grain size distribution in a broad sense (Gordon et al. 2000), it is difficult to connect the current grain sizes to their production sources due to their complex history of growth, destruction, and recycling over short timescales (Jones et al. 2013). In addition, the dust production sources themselves, such as SNe, AGB stars, or Population III stars have changed in relative strength over cosmic timescales (Morgan & Edmunds 2003; Nozawa et al. 2003). Constraints on the dust law can be used to infer the observed dust grain sizes, which is helpful when modeling the evolution of the production of dust grains (e.g., in high-redshift quasars, Nozawa et al. 2015). A better understanding of these mechanisms would help to constrain metal buildup and galactic feedback (Davé et al. 2011; Gall et al. 2011a).

In addition, both the scale and the shape of the dust law affect the interpretation of galaxy SFRs, the evolution of the SFR density, and the evolution of the opacity of the intergalactic medium (IGM). For example, Smit et al. (2014) showed that the measured $z \sim 7$ sSFR changes by nearly an order of magnitude depending on the assumed prescription of dust attenuation. It is clear that new methods must be developed to determine the shape of the dust law in the distant universe.

Our goal in this work is to provide evidence for the dust law at high redshifts using the information from galaxies' rest-frame UV-to-NIR SEDs. We use a Bayesian formalism that marginalizes over stellar population parameters from models of the galaxy SEDs (Salmon et al. 2015). This allows us to measure evidence in favor of one dust law over another for individual galaxies. We show that the favored dust laws are consistent with the galaxies' locations on the IRX–β diagram for a sample of galaxies at $1.5 < z < 3.0$ with mid-IR imaging, where we can verify that the predicted attenuation agrees with the IRX.

This work is organized as follows. Section 2 outlines our photometric and IR data, redshifts, and sample selection, as well as our calculations of IR luminosities and β. Section 3 describes the framework of our SED-fitting procedure, including the stellar population models and dust laws. Section 4 defines the use of Bayes factors as our selection method, and Section 5 defines our parameterization of the dust law. Section 6 shows the main results of the paper, where we use our Bayesian technique to quantify the evidence that star-forming galaxies at $z \sim 1$–2 have a given dust law, using CANDELS *Hubble Space Telescope* (*HST*) and *Spitzer* data spanning the rest-frame UV-to-NIR SED. We then show that the UV color and thermal IR emission (measured from mid-IR data) of these galaxies matches the properties of their predicted dust law. Section 7 discusses the implications and physical origins of our results, as well as comparisons to previous work and dust theory. Finally, Section 8 summarizes our main conclusions. We assume concordance cosmology such that $H_0 = 70$ km s^{-1} Mpc^{-1}, $\Omega_{\rm M,0} = 0.3$, and $\Omega_{\Lambda,0} = 0.7$.

2. DATA, REDSHIFTS, AND SAMPLE SELECTION

2.1. Photometry: CANDELS GOODS Multi-wavelength Data

This work takes advantage of the multi-wavelength photometry from the GOODS North and South Fields (Giavalisco et al. 2004), the CANDELS survey (Grogin et al. 2011; Koekemoer et al. 2011), the WFC3 Early Release Science program (Windhorst et al. 2011), and the Hubble Ultra Deep Field (Beckwith et al. 2006; Ellis et al. 2013; Illingworth et al. 2013; Koekemoer et al. 2013). We define magnitudes measured by *HST* passbands with the ACS F435W, F606W, F775W, F814W, and F850LP as B_{435}, V_{606}, i_{775}, I_{814}, and z_{850}, and with the WFC3 F098M, F105W, F125W, F140W, and F160W as Y_{098}, Y_{105}, J_{125}, JH_{140}, and H_{160}, respectively. Similarly, bandpasses acquired from ground-based observations include the VLT/ISAAC K_s and VLT/HAWK-I K_s bands. We refer to Guo et al. (2013) for more details on the GOODS-S data set, and G. Barro et al. (2016, in preparation) for the GOODS-N data set.

As applied by Salmon et al. (2015), we include an additional uncertainty, defined to be 10% of the flux density per passband of each object. This accounts for any systematic uncertainty such as flat-field variations, point-spread function (PSF), and

aperture mismatching, and local background subtraction. The exact value was chosen from series of recovery tests on semi-analytic models applied by Salmon et al. (2015). Including this additional uncertainty also helps to avoid situations where a given model SED band serendipitously finds a perfect match to an observed low-uncertainty band, creating a biased posterior around local maxima. The additional uncertainty was added in quadrature to the measured uncertainties.

2.2. IR Photometry: Spitzer and Herschel

We use imaging in the IRAC 3.6 and 4.5 μm bands from the *Spitzer* Extended Deep Survey (Ashby et al. 2013) to measure the rest-frame NIR of the galaxy SED. As described by Guo et al. (2011), the IRAC catalog uses the *HST* WFC3 high-resolution imaging as a template and matches to the lower-resolution images using the TFIT software package (Laidler et al. 2007) to measure the photometry.

In order to verify the dust-attenuation law derived from the rest-frame UV-to-NIR data, we require a measure of the rest-frame UV-to-optical light reprocessed by dust and re-emitted in the far IR. Conventionally, the important quantities are the ratio of the observed IR-to-UV luminosities, $L(\mathrm{IR})/L(\mathrm{UV})$, which measures the amount of reprocessed light, and the UV spectral slope, β, which measures the shape of the dust-attenuation curve (e.g., Meurer et al. 1999; Charlot & Fall 2000; Gordon et al. 2000; Noll et al. 2009; Reddy et al. 2010). We used MIPS 24 μm measurements from the GOODS-*Herschel* program (Elbaz et al. 2011), where the GOODS IRAC 3.6 μm data were used as prior positions to determine the MIPS 24 μm source positions. Then, PSF-fitting source extraction was performed to obtain 24 μm fluxes, which we require to be $>3\sigma$ detections for our sample. While we also examined galaxies with *Herschel* PACS and SPIRE 100–250 μm photometry; these data were ultimately not included because they had no effect on the results (see Appendix B).

2.3. Redshifts

To minimize uncertainties in SED fitting owing to redshift errors, we selected objects that have the highest quality spectroscopic redshifts. The spectroscopic redshifts are a compilation (N. Hathi & M. Dickinson 2016, private communication) from several published and unpublished studies of galaxies in GOODS-S (Doherty et al. 2005; Mignoli et al. 2005; Kriek et al. 2008; Vanzella et al. 2008; Popesso et al. 2009; Balestra et al. 2010; Fadda et al. 2010; B. Weiner et al., unpublished) and GOODS-N (Reddy et al. 2006; Daddi et al. 2009). We define the sample of galaxies with high-quality redshifts as the "spec-z" sample, but later we consider the full sample with photometric redshifts, which we call the "phot-z" sample.

The primary goal of this work is to determine the ubiquity of the dust-attenuation law at the peak of cosmic SFR density. When deriving properties of distant galaxies, we must naturally consider how our results are dependent on the assumed redshift of each galaxy. This can be done in two ways. First, we explore how our results depend on redshift accuracy by testing how our results vary if we use photometric redshifts for galaxies rather than their spectroscopic redshifts. Second, we determine how the results of the spec-z sample differ from a larger sample of galaxies with photometric redshifts. The former test addresses how photometric-redshift accuracy in general affects the methods and results, while the latter test addresses whether the photometric-redshift accuracy within a larger sample is sufficient to reproduce the spectroscopic-redshift results. In addition, a photometric-redshift sample can reveal biases in the spec-z sample because the latter is likely biased toward the brighter, bluer galaxies.

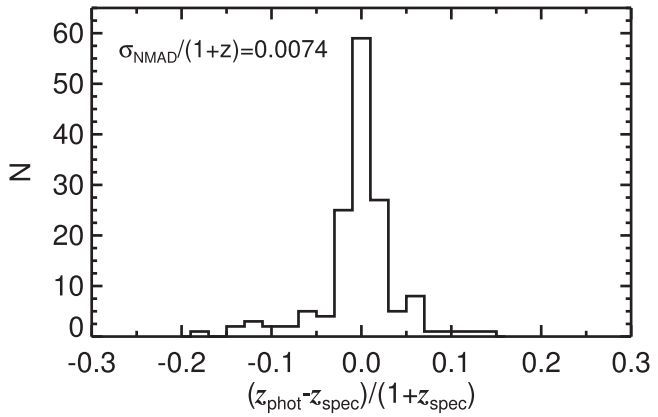

Figure 1. Photometric-redshift accuracy for galaxies that are in both the phot-z and spec-z samples. σ_{NMAD} gives the 68% scatter of the distribution.

We used photometric redshifts that were derived following the methods by Dahlen et al. (2013), who developed a hierarchal Bayesian technique to convolve the efforts of 11 investigators of photometric redshift in the CANDELS team. The photometric-redshift estimates of GOODS-S are taken from Santini et al. (2015) and those of GOODS-N are taken from T. Dahlen et al. (2015, in preparation). The estimates of GOODS-N photometric redshift also take advantage of SHARDS-grism narrow-band data. We take the photometric redshift as the median from the combined full $P(z)$ distributions of nine GOODS-N and six GOODS-S investigators of photometric redshift.

Figure 1 shows the accuracy of the photometric redshifts when compared with spectroscopic redshifts for galaxies where the latter are known. We estimate the photometric-redshift accuracy from the normalized median absolute deviation (Brammer et al. 2008), which gives a 68% scatter of the distribution of $\sigma_{\mathrm{NMAD}}/(1+z) = 0.0074$. In addition, 94% of the sample has a quality of $|z_{\mathrm{phot}} - z_{\mathrm{spec}}|/(1+z_{\mathrm{spec}}) < 0.1$. This gives us confidence that the redshifts of the phot-z sample are well determined.

2.4. Sample Selection

We limited the sample to $z > 1.5$, such that the ACS B_{435} band still samples the rest-frame far UV (FUV, ~1500 Å), which is a crucial portion of the SED when distinguishing between dust laws. Section 6.1 discusses the consequences of a galaxy not having a band close to the FUV, due to the redshift or available photometry. We also required a $z < 3$ limit because the IR selection of sources at higher redshift corresponds to objects with very bright IR luminosities ($\log L_{\mathrm{TIR}}/L_{\odot} < 12.5$), where the frequency of objects dominated by emission from an active galactic nucleus (AGN) increases to ~60% (Nardini et al. 2010). In addition, the upper redshift limit was chosen to avoid significant redshift evolution within the sample.

Applying the redshift range of $1.5 < z < 3.0$ to the sample and requiring 24 μm detections (signal-to-noise ratio $S/N > 3$) produces an initial sample of 65 (554) GOODS-N

and 123 (552) GOODS-S spec-z (phot-z) selected galaxies. A small number (<5% of the spec-z sample and <2% of the phot-z) of objects were identified on or near bright stars and diffraction spikes, as well as at the edges of the image (Guo et al. 2013), and were removed from all samples.

We further identified galaxies that imply the presence of an AGN from their IR or radio data (Padovani et al. 2011; Donley et al. 2012) or if they have known X-ray detections (Xue et al. 2011). This selection removes 6 (52) GOODS-N and 31 (108) GOODS-S sources in the spec-z (phot-z) sample. Our final sample contains 56 (485) GOODS-N and 88 (432) GOODS-S galaxies in the fiducial spec-z (phot-z) sample.

2.5. Calculation of Total Infrared Luminosities

One method to calculate the total infrared luminosity ($L_{\rm TIR}$) involves fitting broadband flux densities to a suite of look-up tables that were derived from templates of local IR-luminous galaxies (Dale et al. 2001; Dale & Helou 2002; Rieke et al. 2009; Elbaz et al. 2011). However, recent work has shown that template fitting can overestimate $L_{\rm TIR}$, especially when the observed bands do not sample the dusty SED well (see Papovich et al. 2007; Overzier et al. 2011). At the redshifts of our sample, 46% of our galaxies lack detections redward of 24 μm (i.e., *Herschel* PACS or SPIRE).

Detailed studies have shown that the rest-frame mid-IR emission is an excellent estimator for $L_{\rm TIR}$ for both local and high-redshift ($z < 2.8$) galaxies once it has been properly calibrated (Wuyts et al. 2008; Rujopakarn et al. 2013, R13 hereafter). This conversion was developed using the fact that the average IR SEDs of galaxies are governed by their IR surface densities (Rujopakarn et al. 2011), allowing bolometric corrections to account for high-redshift emission from poly-aromatic hydrocarbons. For the galaxies in our range of redshift and luminosity, R13 showed that the scatter in $L_{\rm TIR}$ derived from the 24 μm emission is very tight, only 0.06 dex (see R13, their Figure 2). Therefore, we adopted the relation from R13 (their Equation (3)) to derive $L_{\rm TIR}$ for the galaxies in our study using their observed 24 μm emission and redshifts.

The adopted 24 μm conversion was developed under several relevant assumptions: it applies to $z \sim 2$ galaxies that lie on the SFR–stellar mass main sequence (most galaxies in our sample are on the main sequence), the galaxies are not hyperluminous ($L_{\rm TIR} < 10^{13} L_{\odot}$), and the surface density of log $L_{\rm TIR}$ scales linearly with log $L_{\rm TIR}$. These assumptions become important for compact starburst galaxies and ULIRGs (ultraluminous IR galaxies, $L_{\rm TIR}/L_{\odot} > 10^{12}$). Nevertheless, these objects are rare, and fewer than 25% of galaxies have $L_{\rm TIR}/L_{\odot} > 10^{12}$ in both the phot-z and spec-z samples. This fraction of the sample are not the galaxies that drive the results of this work.

As a further check, 54% of the galaxies in our spec-z sample have *Herschel* PACS and/or SPIRE data. The comparison using these data to calculate $L_{\rm TIR}$ can be found in Appendix B, but in short, the results of this work are unaffected by using fits to *Herschel* data instead of the 24 μm conversion to calculate $L_{\rm TIR}$.

The distribution of $L_{\rm TIR}$ is shown in Figure 2 as a function of redshift for all 24 μm detected sources with spectroscopic redshifts, including those within our redshift range. For reference, we also show the SFRs corresponding to a given $L_{\rm TIR}$ following conversion using Equation (8) of R13, which is similar to the conversion of Kennicutt (1998) with factors applied appropriate for a Salpeter (1955) IMF. This figure shows that galaxies in our sample have IR luminosities ranging from 5×10^{10} to 3×10^{12} $L_{\odot}$, consistent with luminosities of LIRGs (luminous IR galaxies).

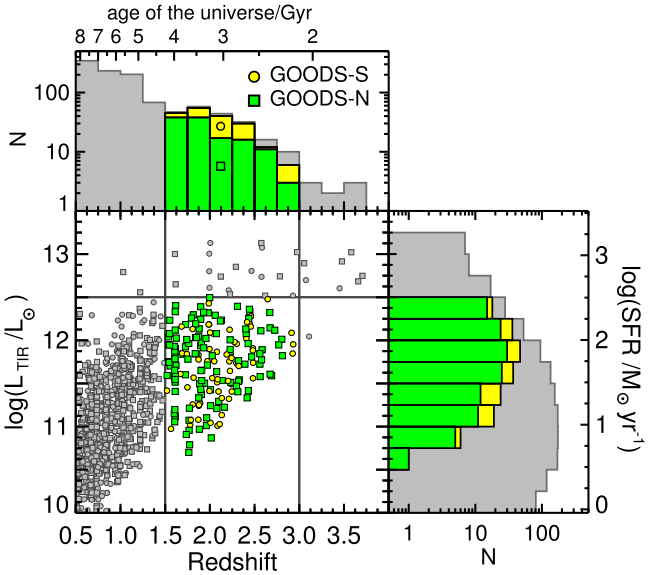

Figure 2. Log of total IR luminosity ($L_{\rm TIR}$), which was determined using a redshift-dependent conversion from $L_{24\,\mu{\rm m}}$, as a function of redshift. Galaxies in our sample lie in GOODS-N (yellow) and GOODS-S (green) and were restricted to log $L_{\rm TIR} < 12.5$ and $1.5 < z_{\rm spec} < 3.0$. The adjacent histograms compare the logarithmic distributions of our sample to the parent sample. For reference, the top and right axes show the age of the universe and the SFR respectively.

2.6. Calculation of the UV Luminosity

We derive the observed UV luminosity, $L_{\rm UV}$, that is, the UV luminosity uncorrected for dust attenuation, as follows. $L_{\rm UV}$ was determined by taking the average luminosity of the best-fit SED in a 100 Å bandwidth centered at 1500 Å. There is little dependence on the choice of SED models, such as the choice of dust law or star formation history (SFH), in determing $L_{\rm UV}$. Similar results are also found when approximating $L_{\rm UV}$ as the luminosity of the observed band closest to rest-frame 1500 Å.

2.7. Calculation of the UV Spectral Slope β

The rest-frame UV slope is an important observational tool due to its relative ease of measurement for galaxies with the highest redshift (even to $z \sim 10$, see Wilkins et al. 2016) and its sensitivity to stellar population age, metallicity, and attenuation by dust. Moreover, β has often been used to estimate the dust attenuation by extrapolating its well-known local correlation with infrared excess (Meurer et al. 1995, 1999). Studies of the origins of the scatter in the IRX–β relation show that it depends on metallicity, stellar population age, SFH, spatial disassociation of UV and IR components, and the shape of the underlying dust-attenuation curve, including the presence of the 2175 Å absorption feature (Gordon et al. 2000; Buat et al. 2005, 2010; Reddy et al. 2006; Muñoz-Mateos et al. 2009; Boquien et al. 2012). This raises concerns about generalizing the IRX–β relation to higher redshifts (e.g., see the discussion by Casey et al. 2014b).

Historically, the methods used to calculate β have been entirely dependent on the available data set. In the absence of UV continuum spectroscopy (the original method to determine

β, Calzetti et al. 1994), we must calculate β from the UV colors provided by broadband photometry. Specifically, we calculated β from the best-fit SED following the methods of Finkelstein et al. (2012). We favor this method over a power-law fit to the observed photometric bands for the following reasons.

First, we ran simple tests on the stellar population models to recover the input β with a power-law fit to the bands with central wavelengths in the range rest-frame $1200 < \lambda < 3000$ Å. The true β is determined from stellar population models by Kinney et al. (1996), using the spectral windows defined by Calzetti et al. (1994) after applying a range of $E(B-V)$. This method produced a systematic offset at all redshifts such that $\beta_{\rm true} = \beta_{\rm phot} - 0.1$, and at some redshifts the recovery is off as much as $\Delta\beta = -0.5$.

Second, Finkelstein et al. (2012) saw a similar offset and scatter in recovering β from a single color or power-law fit. They promoted the calculation of β by using UV-to-optical photometry to find the best-fit SED and using the UV spectral windows of Calzetti et al. (1994) to determine β. Their simulations reported a better recovery of $\beta_{\rm true}$ with no clear systematics and a scatter of $\Delta\beta = \pm 0.1$ for galaxies at $z = 4$. We therefore used the best-fit model to calculate β, assuming a constant SFH and a starburst dust law (Calzetti et al. 2000) (see Appendix C in this paper, which shows that the results are not sensitive to changing the derivation of β to be a power-law fit to the photometry in the rest-frame UV).

One may be concerned that the adopted method makes β sensitive to the assumed dust law of the SED models. However, the best-fit SED will always provide a close match to the UV colors so long as the assumed dust law does not have any extreme features such as the excess of absorption at 2175 Å or the almost broken power-law rise in the far UV of the extinction curve of Pei (1992). We find similar results when calculating β from the best-fit SED when we allow the shape of the dust law to vary as a new parameter in Section 5.

3. MODELING STELLAR POPULATIONS

The bulk of the methods and procedures of the SED fitting are described by Salmon et al. (2015), which we summarize here including recent changes. The SED fitting is Bayesian in nature, offering a mechanism to determine the conditional probability for each desired physical property of the galaxy.

3.1. Bayesian Methods

Using Bayes' theorem,

$$P(\Theta'|D) = P(D|\Theta')\,P(\Theta')/P(D), \quad (2)$$

we determine the posterior, $P(\Theta'|D)$, with parameters $\Theta' = (\Theta\{t_{\rm age}, E(B-V), Z\}, M_\star)$ and data, D, under the a priori probability of the parameters or simply the "prior," $P(\Theta')$. The likelihood, $P(D|\Theta')$, is determined in the usual way using χ^2 statistics (i.e., Equation (2) of Salmon et al. 2015). The unconditional marginal likelihood of the data, $P(D)$, often referred to as the Bayesian evidence[15], normalizes the posterior such that the integrated posterior across all parameters is equal to unity (Jeffreys 1961; Heckerman 1995; Newton et al. 1996):

$$\text{Bayesian evidence} \equiv P(D) = \int_\Theta P(D|\Theta)\,P(\Theta)\,d\Theta. \quad (3)$$

Calculating the unconditional marginal likelihood is a way to eliminate the parameters Θ from the posterior (in Equation (2)) through integration, leaving us with the probability of seeing the data D given all possible Θ (Kass & Raftery 1995). The importance of the marginal likelihood will be discussed further in Section 4.

Posteriors on individual parameters can be determined by marginalizing over nuisance parameters. The strength of this Bayesian approach is that the marginal probability of a given parameter is conditional to the probability from the nuisance parameters. For example, the posterior on $E(B-V)$ is conditional to the probability contribution from all stellar population ages, metallicities, and SFHs. This approach is an alternative to using parameter results taken from the best-fit (minimum χ^2) model SED because it relies on posterior integration instead of likelihood maximization. The disadvantage of the latter is that small differences in χ^2 or an underrepresentation of measurement uncertainties can result in best-fit models that are sporadic across the parameter space, making results highly dependent on the assumptions of the SED template (see Figures 20 and 21 of Salmon et al. 2015). We therefore favor using the median of each parameter's marginalized posterior over results determined from the best-fit model, as supported by recent literature (Smith & Hayward 2015; Song et al. 2016; Tanaka 2015).

3.2. Stellar Population Models

Table 1 shows the ranges, quantity of values considered, and priors of the SED fitting parameters. Each combination of age, metallicity, and $E(B-V)$ produces an SED shape and associated χ^2. The parameter space was constructed following the listed priors on each parameter. We used stellar population synthesis models of Bruzual & Charlot (2003) with the addition of nebular emission lines assuming escape fraction from the ionizing continuum of $f_{\rm esc} = 0$ (Salmon et al. 2015). We assumed a Salpeter (1955) initial mass function and H I absorption from line-of-sight IGM clouds according to Meiksin (2006). The IGM attenuation model of Meiksin (2006) includes higher order Lyman transitions. Nevertheless, the assumption of IGM attenuation has minimal effect on the results because few galaxies have photometry covering wavelengths blueward of 1216 Å.

The range of $E(B-V)$ extends below zero for two reasons. First, consider the example where a Gaussian-shaped posterior for parameter x peaks at $x = 0$, but all probability at $x < 0$ is set to zero. The x corresponding to the median probability of such a posterior would be biased to $x > 0$, an artifact of the choice of parameter space. This was pointed out by Noll et al. (2009), who showed a bias to Bayesian estimates of certain parameters, especially parameters such as $E(B-V)$ whose posterior often peaks at the edge of the parameter space. Second, negative values of $E(B-V)$ are not necessarily unphysical. There are some, albeit rare, situations where isotropic scattering by dust in face-on galaxies can produce an enhancement of optical light (i.e., $A_V < 0$ Chevallard et al. 2013).

We also considered how our results are dependent on the assumed shape of the SFH. The SFH is known to be a poorly constrained parameter in the fitting process (e.g., Papovich et al. 2001; Noll et al. 2009; Buat et al. 2012; Reddy et al.

[15] The Bayesian evidence is occasionally denoted by Z. We adopt the formal definition, $P(D)$, to avoid confusion with the conventional astronomical symbol for metallicity.

Table 1
SED Fitting Parameters

Parameter	Quantity	Prior	Relevant Sections
Redshift	fixed	spectroscopic redshifts, $1.5 \leqslant z_{\rm spec} \leqslant 3.0$	Sections 2.3, 6.2
	fixed	photometric redshifts, $1.5 \leqslant z_{\rm phot} \leqslant 3.0$	Sections 2.3, 6.3
Age	100	10 Myr to $t_{\rm max}$[a]	...
Metallicity	5	$Z = 0.02, 0.2, 0.4, 1.0, 2.5\,Z_{\odot}$	...
$E(B-V)$[b]	85	Linear, $-0.6 < E(B-V) < 1.5$, $\Delta E(B-V) = 0.025$	Section 3.3
Attenuation prescription	fixed	starburst (Calzetti et al. 2000) or SMC92 (Pei 1992)	Sections 3.3, 6.2.2
	11[c]	$-0.6 < \delta < +0.4$, in steps of $\Delta\delta = 0.1$	Sections 5, 6.3.2
$f_{\rm esc}$	fixed	0	—
Star formation history[d]	fixed	100 Gyr (constant)	Section 3.2
	10	$\pm\tau = 0.1, 0.3, 1, 3, 10$ Gyr	Section 3.2

Notes.
[a] The lower end of this range represents the minimum dynamical time of galaxies in our redshift range up to $t_{\rm max}$, which is the age of the universe for the redshift of each object, which is up to 4.2 Gyr at $z \sim 1.5$.
[b] We fit to a range of color excess values, $E(B-V)$. This scales the dust-attenuation curve to achieve a wavelength-dependent attenuation, $A(\lambda) = k(\lambda)E(B-V)$.
[c] This parameterized dust law is a power-law deviation from the starburst dust law, similar to Noll et al. (2009) (see Section 5 for a detailed definition).
[d] The star formation history is defined as $\Psi(t) = \Psi_0 \exp(t/\tau)$ such that an SFR that increases with cosmic time has a positive e-folding time, τ. When the SFH is allowed to vary as a fitted parameter, we consider rising and declining histories (positive and negative τ) seperately. The long e-folding time of $\tau = 100$ Gyr is effectively a constant star formation history.

2012; Mitchell et al. 2013). While it is not the motivation of this work to accurately fit the SFH for individual galaxies, assuming a fixed history may reduce flexibility in the parameter space and overstate the perceived evidence between different dust laws. We therefore considered three scenarios for the SFH: constant, rising, and declining exponentially with cosmic time, with ranges for the latter two cases described in Table 1. We take the assumption of a constant history as our fiducial model, and we show in Appendix D that our main results are unchanged if we instead adopt rising or declining SFHs.

The stellar mass was treated differently than the individual parameters Θ. It is effectively a normalization of the SED, given the mass-to-light ratio associated with the SED shape; hence the distinction in Section 3.1 between Θ, which represents the parameters that actually drive the goodness of fit, and Θ', which is those parameters and their associated stellar mass. In this manner, the posterior in stellar mass was determined by integrating the posterior rank-ordered by stellar mass to achieve a cumulative probability distribution in stellar mass such that the median is defined where the cumulative probability is equal to 50%.

3.3. Known Dust Attenuation Curves

The dust law was fixed during the fitting process (along with the redshift, escape fraction, and SFH), although we individually considered a variety of commonly used dust laws. The curves of these dust laws are shown in Figure 3 and include those of the empirically derived attenuation for local starburst galaxies (Calzetti et al. 2000), the Milky Way extinction (which showcases the strong 2175 Å dust absorption feature, Gordon et al. 2003), an empirically derived attenuation for $z \sim 2$ star-forming galaxies ("MOSDEF," Reddy et al. 2015), and two interpretations of the SMC extinction: SMC92 (Pei 1992) and SMC03 (Gordon et al. 2003), hereafter.

In Figure 4, several dust attenuation and extinction laws from Figure 3 are shown on the plane of infrared excess, IRX, and UV

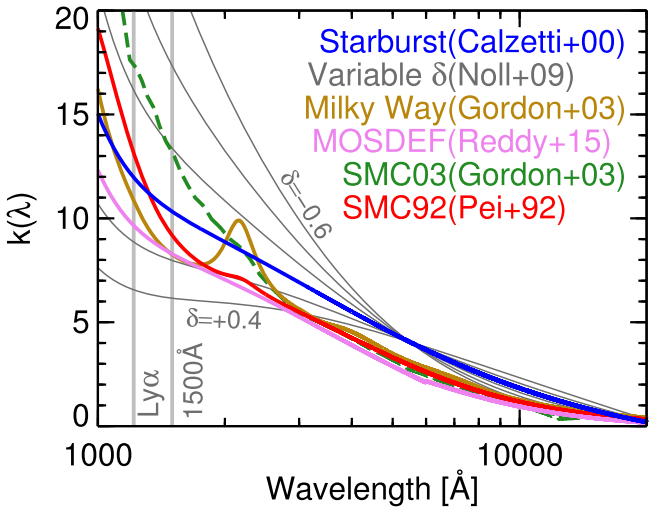

Figure 3. A variety of common dust laws shown by their total-to-selective extinction or attenuation as a function of wavelength. The derivation in Pei (1992) of the SMC extinction (red, SMC92) will be used in this work to compare to the starburst prescription derived by Calzetti et al. (2000) (blue). Other dust laws are also shown including the MOSDEF (pink) attenuation curve derived from $z \sim 2$ galaxies (Reddy et al. 2015), and the Milky Way (gold) and SMC (SMC03, green, dashed) extinction curves derived by Gordon et al. (2003). In addition, we consider power-law deviations from the starburst curve (Equation (7)) to be more ($+\delta$) or less ($-\delta$) gray. The wavelengths of 1500 Å and the Lyα emission line are shown for reference.

slope, β. Each dust law's IRX–β relation represents the predicted location of a variety of stellar populations that have been reddened according to their given dust-attenuation or dust-extinction curve. Creating these relations requires several assumptions about the intrinsic stellar populations, which are manifest as an increase in the relation's width. First, we obtained a library of stellar populations from Bruzual & Charlot (2003) with a range of ages (50 Myr to 1 Gyr), star formation histories (SFR $\sim e^{t/\tau}$, where 1 Gyr $< \tau <$ 100 Gyr), and metallicities ($0.02\,Z_{\odot} < Z <$

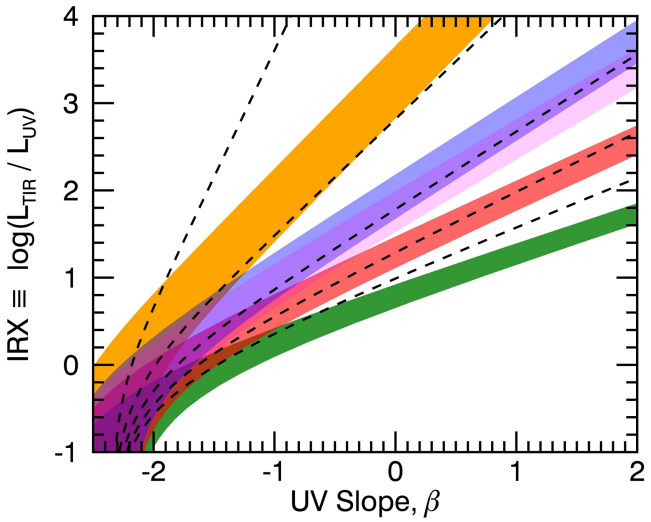

Figure 4. Predicted locations of galaxies with different dust laws on the plane of the UV slope β and infrared excess ($L_{\rm TIR}/L_{\rm UV}$). The colored swaths correspond to the same dust laws as in Figure 3, clockwise from top left: Milky Way, starburst, MOSDEF, SMC92, and SMC03. The width of each IRX–β relation accounts for the scatter in the intrinsic β from the effects of stellar population age (50 Myr to 1 Gyr), SFH (SFR $\sim e^{-t/\tau}$, with 1 Gyr $< \tau <$ 100 Gyr), and metallicity ($0.02\ Z_\odot < Z < 2.5\ Z_\odot$). The dashed lines show the relations according to the parameterized dust law (see Section 5) with (clockwise from left) $\delta = +0.4, +0.2, 0.0, -0.2, -0.4$.

2.5 $Z_\odot$). Then, we subtracted the dust-attenuated SED from the intrinsic SED and integrated the residual across all wavelengths to obtain an estimate of the bolometric IR luminosity for these models. We made the approximation that the calculated IR luminosity of each model is representative of $L_{\rm TIR}$, under the assumption that all attenuated UV-to-NIR light is completely reprocessed to produce the total IR luminosity. $L_{\rm UV}$ and β for these models were calculated using the same methods as used on the best-fit SEDs of the data (in Sections 2.6 and 2.7, respectively).

From this framework, each dust model in Figure 4 has a width in the IRX–β plane that is a product of the range in the stellar population parameters (age, metallicity, SFH), which affects both IRX and β and produces the scatter illustrated by the colored swath. The left edge represents younger, low-metallicity, and maximally blue stellar populations, while the right edge extends toward older, metal-rich, and intrinsically red stellar populations. With increasing steps of $E(B-V)$ (moving up each IRX–β relation), a steeper dust law will redden the SED faster and therefore produce less IRX at a given β when compared to grayer, starburst-like dust laws (Siana et al. 2009). In addition, the presence of a dust absorption feature at 2175 Å, such as is found in the dust law for the Milky Way, will produce a significant excess of IR emission without significantly contributing to the reddening (although this depends on the manner in which β is determined, see Kriek & Conroy 2013). These IRX–β relations provide an observational basis from which to distinguish between dust-attenuation curves.

4. DISTINGUISHING BETWEEN DUST LAWS WITH BAYES FACTORS

Determining the shape of the dust-attenuation curve from broadband data is nontrivial. Broadband SED fitting is fraught with parameter degeneracies, a product of several physical mechanisms that conspire to produce similar SED shapes (e.g., stellar population age, metallicity, SFH, and dust attenuation; e.g., Papovich et al. 2001, 2011; Lee et al. 2010, 2011; Walcher et al. 2011; Pacifici et al. 2012; Pforr et al. 2012, 2013; Mitchell et al. 2013). As mentioned in Section 3, these degeneracies spawn biases in simple χ^2 tests of likelihood ratio because best-fit models are more sensitive to assumptions about the SED template such as the inclusion of nebular emission lines, changing the assumed dust curve, and/or the degeneracies within the parameters themselves (Tilvi et al. 2013; Salmon et al. 2015).

To distinguish between dust laws, we should consider all parameters, Θ, as nuisance parameters, such that the fully marginalized parameter space contains probability contributions from all Θ. We are then left to quantify the difference between the fully marginalized posteriors under their respective assumptions of non-parametric dust laws. In order to achieve this, we consider the posterior in Bayes theorem (Equation (2)) as being further conditional to a model assumption exterior to the fitting process (in this case, the assumed dust-attenuation curve, k_λ). Then we may determine the odds that the hypothesis of one dust-attenuation curve is correct over another. The ratio of a posterior assuming dust-attenuation curve k_λ^1 and a posterior assuming dust-attenuation curve k_λ^2 is therefore given by

$$\frac{P(\Theta', k_\lambda^1|D)}{P(\Theta', k_\lambda^2|D)} = \frac{P(D|\Theta', k_\lambda^1)}{P(D|\Theta', k_\lambda^2)} \times \frac{P(\Theta'|k_\lambda^1)}{P(\Theta'|k_\lambda^2)},$$
$$\text{or} \qquad \text{posterior odds} = \text{Bayes factor} \times \text{prior odds}. \tag{4}$$

The term in the middle is referred to as the Bayes factor (Jeffreys 1935, 1961; Kass & Raftery 1995). In practice, we may write the Bayes factor as a ratio of the marginal likelihoods (see Sutton & Abrams 2001 for a similar definition). Combining the definition in Equation (3) with the conditions in Equation (4), we obtain the plausibility that one dust-attenuation curve is more likely given another, marginalized over all parameters:

$$\text{Bayes factor} \equiv B_{12} = \frac{P(D|k_\lambda^1)}{P(D|k_\lambda^2)}. \tag{5}$$

Kass & Raftery (1995) offered descriptive statements for Bayes factors in order to denominate several standard tiers of scientific evidence. These were defined using twice the natural logarithm of the Bayes factor, which we will call the Bayes-factor evidence, ζ:

$$\text{Bayes-factor evidence} \equiv \zeta = 2 \cdot \ln B_{12}$$
$$\zeta = 2 \cdot \ln \frac{\int_\Theta P(D|\Theta', k_\lambda^1)\, P(\Theta'|k_\lambda^1)\, d\Theta}{\int_\Theta P(D|\Theta', k_\lambda^2)\, P(\Theta'|k_\lambda^2)\, d\Theta}. \tag{6}$$

We adopt the significance criteria of Kass & Raftery (1995), who define the evidence to be "very strong" ($\zeta > 10$), "strong" ($6 < \zeta < 10$), or "positive" ($2 < \zeta < 6$) toward k_λ^1 (and equivalent negative values for evidence toward k_λ^2). Intuitively, because the Bayesian evidence $P(D)$ is proportional to the integral over the likelihood (Equation (3)), a model that produces a better fit to the data (low χ^2) will yield a higher $P(D)$, making $|\zeta|$ larger in the case where one dust law is more likely than another.

Throughout this paper, we refer to galaxies with high $|\zeta|$ as having strong Bayes-factor evidence toward a given dust law. However, we caution that Bayes factors do not necessarily mandate which of two models is correct but instead describe the evidence against the opposing model. For example, a galaxy with very strong evidence toward model 2 (e.g., $\zeta \approx -20$ according to Equation (6)), promotes the *null hypothesis* that model 1 is correct. Formally, it does not say that model 2 is the correct model, but promotes the rejection of model 1 (and vice versa). In the next section, we address this subtlety with a direct parameterization of the dust-attenuation curve in order to confirm whether the Bayes-factor evidence is indeed pointing toward the appopriate dust prescription.

5. PARAMETERIZING THE DUST LAW

While it is instructive to search for the evidence that galaxies have one of the empirically or physically motivated dust laws from Section 3.3, there is no guarantee that these dust laws apply to all galaxies, particularly at high redshifts. We therefore adopted an alternative model for the dust attenuation, where we parameterize the dust law in the SED-fitting process. The parameterization allows a smooth transition between the different dust laws. Following Kriek & Conroy (2013), we allowed the dust-attenuation curve to vary as a tilt from the starburst curve of Calzetti et al. (2000) similar to the parameterization provided by Noll et al. (2009). This paramaterized dust law, which is a purely analytical interpretation of how the dust-attenuation curve may be adjusted, is

$$A_{\lambda,\delta} \equiv E(B-V) k_{\lambda}^{\rm SB} \, (\lambda/\lambda_{\rm V})^{\delta}. \quad (7)$$

This definition returns the starburst attenuation curve, $k_{\lambda}^{\rm SB}$, when $\delta = 0$, a steeper, stronger attenuation in the FUV when $\delta < 0$, or a flatter, grayer attenuation across UV-to-NIR wavelengths when $\delta > 0$. Examples of these dust laws are shown in Figure 3. We chose a parameter space with a range $-0.6 < \delta < +0.4$ in steps of $\Delta\delta = 0.1$ (see Table 1). This range brackets the range of dust laws observed in the literature. In comparison, SMC92 is slightly steeper than the starburst curve across UV-to-NIR wavelengths, similar to $\delta \approx -0.1$, but is much steeper at $\lambda \lesssim 1500$ Å, similar to $\delta \approx -0.5$.

Given the set of dust laws, we can marginalize over all other parameters Θ to obtain the posterior on δ for each galaxy. This process is the same as the marginalization in Equation (3), where we marginalize over all Θ to obtain the full marginal likelihood, except that we have added an additional parameter δ. In some cases δ may be poorly constrained, and the posterior will be very broad. This is to be expected, as there is similarly a population of galaxies for which the Bayes factor is unable to return significant evidence. The results of fitting to δ are described in Sections 6.2.2 and 6.3.2.

Equation (7) assumes that there is no additional contribution from the 2175 Å absorption feature, which is a hallmark of the dust-attenuation curve of the Milky Way (Gordon et al. 2003) and is likely caused by absorption from polycyclic aromatic hydrocarbons. Although there is evidence of the 2175 Å feature in high-redshift quasars (Noterdaeme et al. 2009), gamma-ray-burst host galaxies (Elíasdóttir et al. 2009), and star-forming galaxies (Noll et al. 2007; Buat et al. 2011), its strength and prevalence in distant galaxy populations remain uncertain (Buat et al. 2012). As we discuss below (Section 6.3.2), we tested for indications of the 2175 Å feature in the dust law and found no substantive evidence for it based on our model fits to the broadband data. We therefore did not include the 2175 Å feature in our modeling. Introducing it would add another parameter to the dust law (see Kriek & Conroy 2013).

6. THE NON-UNIVERSALITY OF DUST LAWS AT $z \sim 2$

6.1. Relevant Spectral Features

Figure 5 shows the SED of a single galaxy in the spec-z sample that has strong Bayes-factor evidence promoting a starburst dust-attenuation law. The SED features that drive the differences in likelihood between the two dust assumptions are subtle. In general, the rest-frame UV flux (1200 Å $\lesssim \lambda \lesssim$ 1400 Å), which at the redshift range of this work is either the B_{435} or V_{606} filter, catches the wavelength where the dust laws differ the most. For galaxies like the example in Figure 5, the rest-frame optical-to-NIR SED suggests a highly attenuated stellar population (high $E(B-V)$), yet the flux from the rest-frame FUV band is brighter than the prediction when assuming SMC92 dust. This results in a lower likelihood for SMC92 models than for models that assume starburst dust. This is true even when accounting for the contribution from Lyα emission in the models or variations in the assumed SFH. The likelihood difference, when marginalized over all parameters, is reflected in the Bayes-factor evidence.

Figure 6 shows the SED of a single galaxy in the spec-z sample that has strong Bayes-factor evidence promoting an SMC92 dust-extinction law. For this galaxy, the rest-frame optical-to-NIR SED suggests a stellar population with relatively low levels of attenuation (low $E(B-V)$). However, there is a subtle decrease in the rest-frame FUV emission, which the starburst attenuation has difficulty matching simultaneously with the rest of the SED, resulting in a lower overall likelihood than the SMC92 assumption. Again, this likelihood difference is reflected in the Bayes-factor evidence.

One potential alternative explanation for the shape of these SEDs is a two-component stellar population: a young burst of star formation producing O- and B-type stars that dominate the rest-frame UV and an already present intermediate-age population that dominates the rest-frame optical-to-NIR SED. As shown in the single-parameter likelihood distributions of Figures 5 and 6, the exponential SFH is a poorly constrained parameter with this data set. Folding in additional SFH parameters will require data with a higher wavelength resolution of the SED in order to overcome its degeneracies with age, metallicity, and the tilt and scale of dust attenuation.

6.2. Results from the Spectroscopic Redshift Sample

6.2.1. Bayes Factors on the IRX–β Relation: spec-z Sample

Figure 7 shows the selection of Bayes-factor evidence for individual galaxies as a function of stellar mass. As expected, most galaxies lack enough evidence from their broadband data alone to distinguish their underlying dust law. However, there are examples of galaxies that display strong evidence toward having an SMC-like or starburst-like attenuation. Figure 7 also shows the plane of IRX–β, where the total infrared luminosities were calculated as described in Section 2.5 and β as in Section 2.7. As noted in Figures 5 and 6, the band closest to the Lyα is the most sensitive to determining the evidence toward a

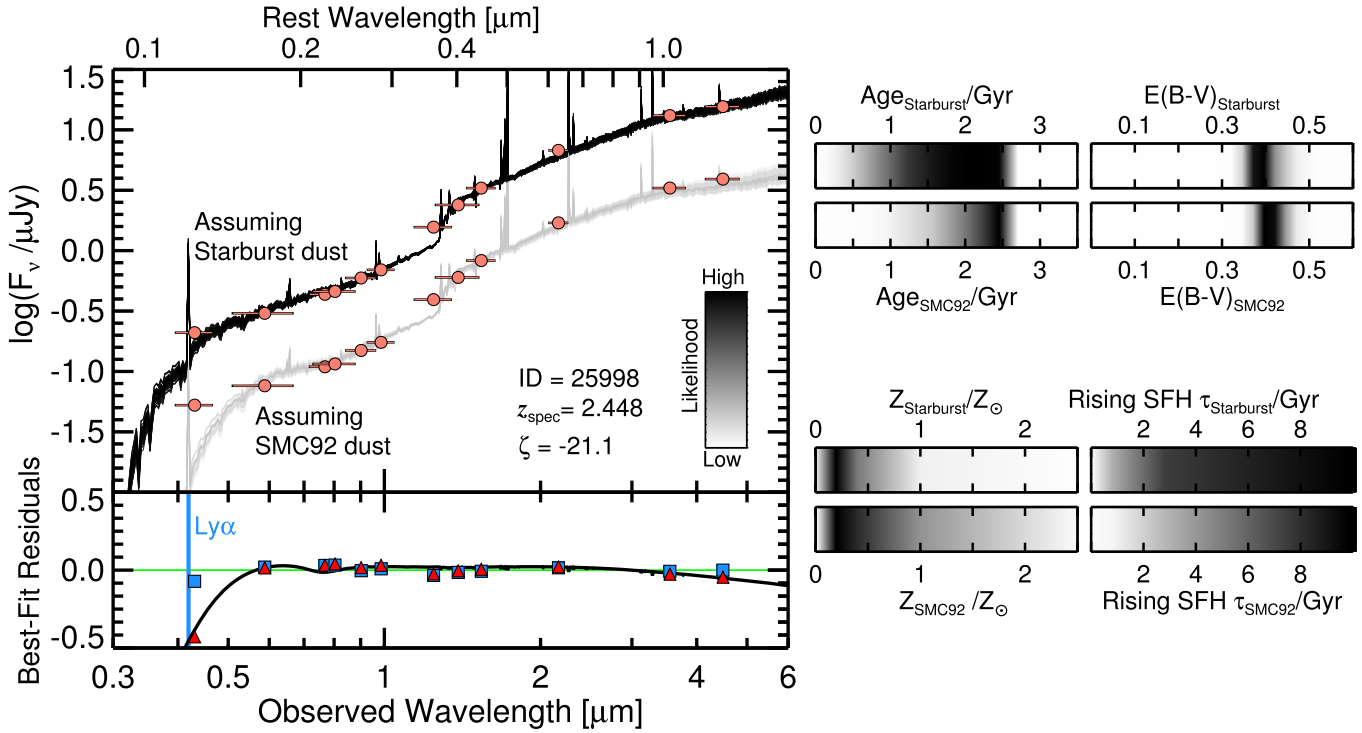

Figure 5. SED of a galaxy in our spec-z sample with strong Bayes-factor evidence ($\zeta = -21$) toward a starburst-like attenuation. The salmon-colored photometric data points are shown twice, with the second set offset by 0.6 dex for clarity. The 50 most likely SEDs are shown, scaled in opacity such that darker curves represent higher likelihood up to the best-fit model, under an assumed starburst (upper) or SMC92 (lower) dust law. The black curve in the lower panel shows the log-difference residual of the best-fit SED under each dust assumption, and the average residual of the data and the 50 best-fit starburst (SMC92) model fluxes in blue squares (red triangles). The residuals of the best-fit SEDs are shown in the lower panel. The bars to the right show the marginalized posteriors of individual parameters, with darker regions denoting higher likelihood. For galaxies with very red SEDs across rest-frame $\lambda = 0.2$–2 μm (the inferred $E(B-V)$ is high) the UV-steep SMC92 dust law is incapable of producing high-likelihood models that match both the $B_{435} - V_{606}$ color and the red rest-frame NIR color. This leads to the large difference in Bayesian evidence and the low Bayes-factor evidence, ζ.

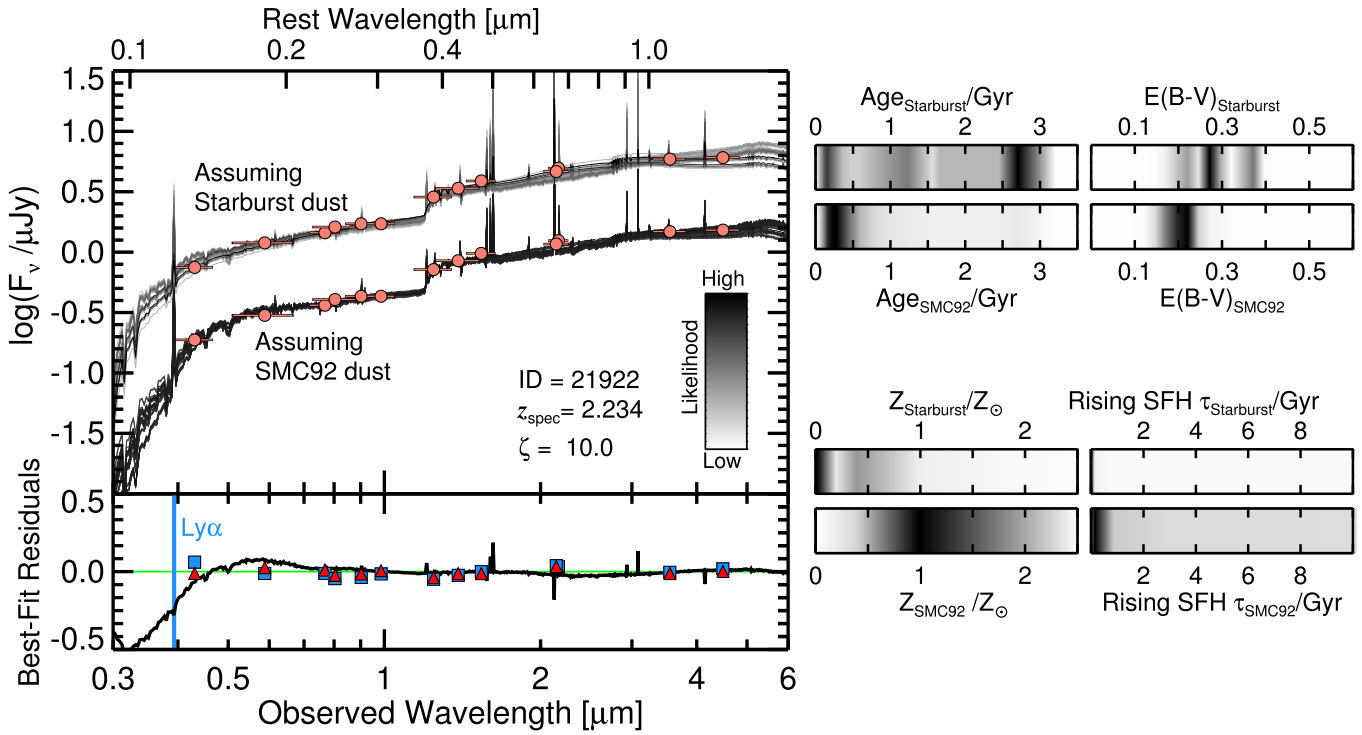

Figure 6. SED of a galaxy that has strong Bayes-factor evidence ($\zeta = 10$) toward an SMC92-like dust-attenuation law. The data are shown twice for fits under each dust assumption, offset by 0.6 dex for clarity. The results between assuming starburst and SMC92 attenuations are subtle; when most of the SED (rest-frame $\lambda = 0.2$–2 μm) suggests relatively low values of $E(B-V)$, the assumption of a starburst law does not produce as many models with significant likelihood as the SMC92 law that are capable of reproducing both the red $B_{435} - V_{606}$ color and the rest-frame NIR color. The resulting difference in likelihood is reflected in the Bayes-factor evidence, ζ.

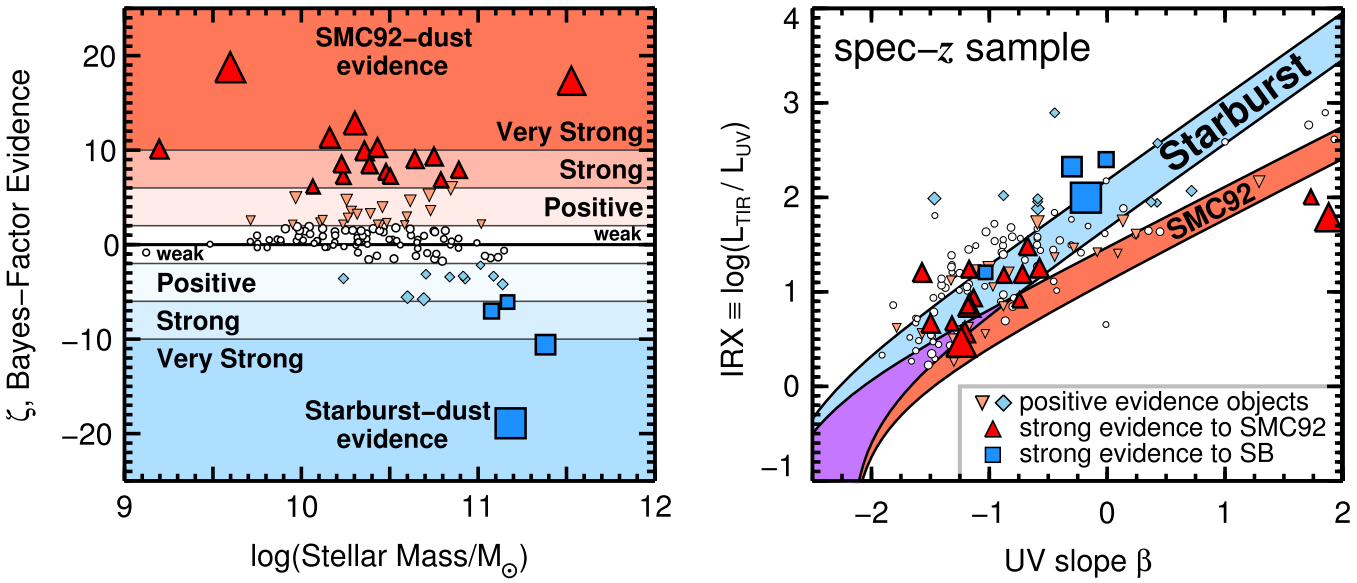

Figure 7. Left: The Bayes-factor evidence as a function of stellar mass for galaxies in the spec-z sample with $1.5 \leqslant z \leqslant 2.5$ and MIPS 24 μm detections of S/N > 3. Darker shaded regions indicate levels of increasing evidence and are used to select objects that show strong preference for SMC92 (red triangles) or starburst (blue squares) dust curves. No mid-IR information was used in the left panel; these values were achieved by modeling rest-frame UV-to-NIR fluxes only. Right: Measured IR excess vs. UV slope to test results inferred from the UV/NIR SED. Prediction curves from stellar population models for SMC92 (red) and starburst (blue) dust laws are shown. Objects selected by the strength of their Bayes-factor evidence follow the curve of their predicted dust-attenuation curve with some scatter. The independent measurements of the IRX–β relation supports the Bayesian evidence from the modeling of the UV/NIR SED: galaxies with (very) strong Bayes-factor evidence follow the correct IRX–β relation.

given dust law because it is at the wavelength where the dust prescriptions differ the most.

The Bayes-factor evidence for different dust laws is consistent with the galaxies' positions in the IRX–β plane. The Bayes-factor evidence was derived from the rest-frame UV-to-NIR photometry and shows that some galaxies have very strong evidence against the starburst law or SMC92 law. Those same galaxies have IRX–β measurements consistent with the Bayes-factor evidence. This is significant because the $L_{\rm TIR}$ data provide an independent measure of the dust law.

Though the results of Figure 7 seemingly identify galaxies with two types of underlying dust scenarios, we must recognize the possibility that neither dust-attenuation curve is appropriate, even for some of the objects with the strongest evidence. In the next section, we pursue this possibility using the methods described in Section 5 to parameterize the dust-attenuation curve as a new variable in the fitting process.

6.2.2. Fitting the Curve of the Dust Law: spec-z Sample

Figure 8 shows the results of fitting to the parameterized dust-attenuation curve (Equation (7)). The selection of galaxies with strong evidence toward a starburst-like dust-attenuation curve agrees with the results from fitting to the dust-attenuation curve directly. Similarly, SMC-like galaxies are better described by a steeper dust-attenuation curve ($\delta < -0.2$), albeit to varying degrees. The galaxies selected to have strong evidence toward an SMC92 dust law exhibit a marked steepness in their fitted dust-attenuation curve that contrasts with a starburst dust law.

In Section 4, we mentioned how the Bayes factor is formally promoting the *null hypothesis* of the opposing model. For example, the Bayesian evidence formally does not favor model 1, but provides evidence against the competing model 2 compared to model 1. However, taken together, the results in Figure 8 imply that galaxies with negative δ really do have steeper attenuation curves like that of the SMC92. In this case, we may consider the evidence toward the null hypothesis of the opposing dust law as being the same as positive evidence for the hypothesis of the dust law itself.

One of the main results of this work is seen in Figure 9: there is a strong relation between $E(B-V)$ and δ. Figure 9 shows the derived values of $E(B-V)$ and δ for galaxies with high Bayes-factor evidence. Because both axes are derived quanties with associated posteriors, we combine the posteriors into a two-dimensional posterior for the whole sample. In both cases, a clear trend emerges such that galaxies with steeper, SMC-like dust laws also have lower levels of attenuation, whereas galaxies with high attenuation have grayer, starburst-like dust laws. This correlation agrees with the IRX–β relation in Figure 4; galaxies with low IRX are expected to have steeper dust laws.

6.3. Results from the Photometric Redshift Sample

6.3.1. Bayes Factors on the IRX–β Relation: phot-z Sample

Figure 10 shows the IRX–β plot for the phot-z sample (see Section 2.3). The phot-z sample includes galaxies from the spec-z sample but with their redshifts assigned to their photometric-redshift value. Figure 10 also shows the results from directly substituting the photometric redshifts for the spec-z sample, in order to explore how photometric-redshift accuracy can affect the main results. The calculation of the UV slope is also sensitive to the photometric-redshift uncertainty because the bands used to find the slope may differ for large changes in redshift (see the details on the calculation of β in Section 6.2.1). It is plausible that galaxies in the spec-z sample have better photometric-redshift accuracies than those for the full phot-z sample. However, we assume that the selection bias to the right panel of Figure 10 is negligible because the trends

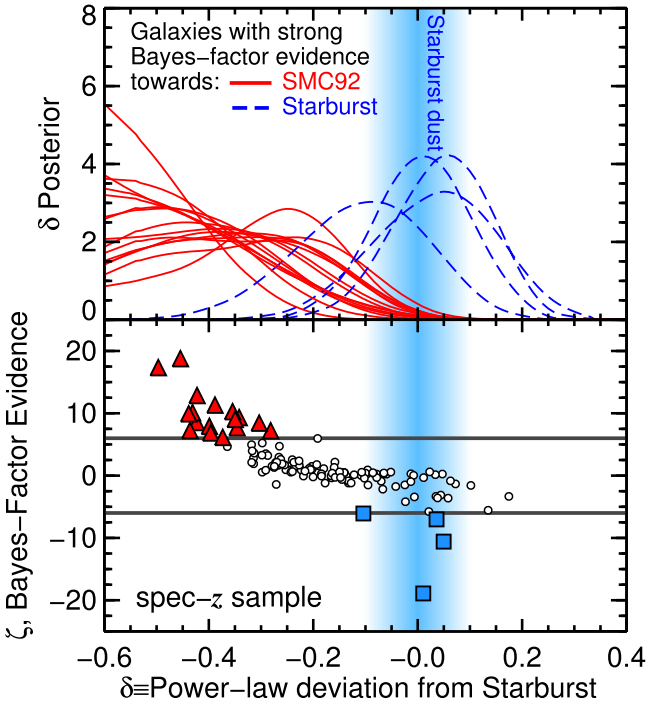

Figure 8. Top: The posterior probability of the fitted parameter δ, the power-law deviation from a starburst (Calzetti et al. 2000) dust-attenuation curve, for galaxies in the spec-z sample and a broadband filter near Lyα. Each curve represents a galaxy that was selected in Figure 7 as having strong Bayes-factor evidence toward an SMC-like (red, solid) or a starburst-like (blue, dashed) dust-attenuation curve. The width of the blue hazed region shows the typical 1σ uncertainty in the median value of δ, centered on $\delta = 0$ where a galaxy would have a starburst dust-attenuation curve. Bottom: The evidence from the Bayes factors between the SMC92 and starburst dust laws as a function of the δ posterior median. Symbols' shapes and colors are the same as in Figure 7. The Bayes factors of galaxies with strong evidence broadly agree with the median δ, as would be expected.

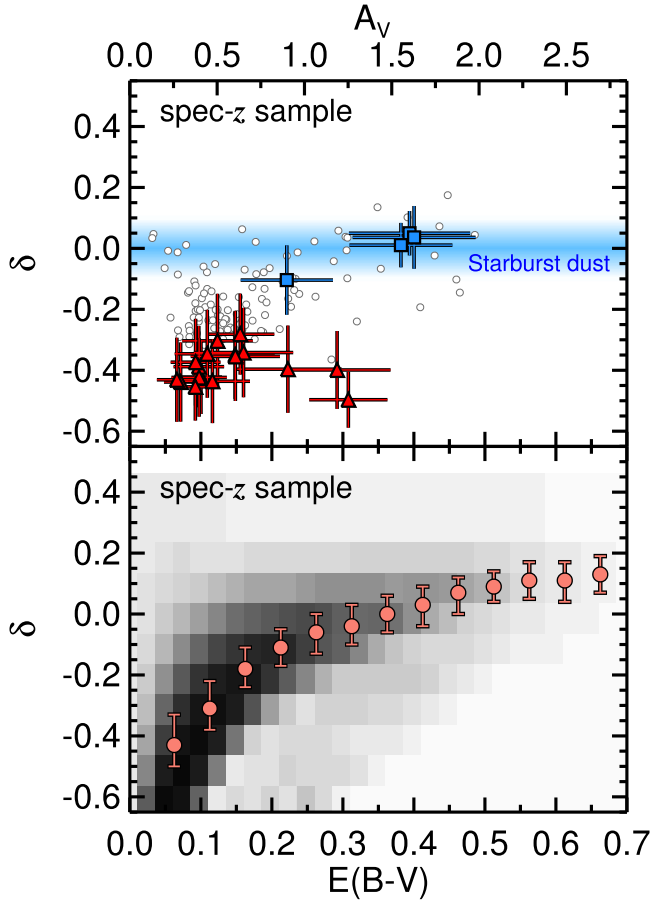

Figure 9. Top: The median of the posterior on the tilt of the dust-attenuation curve, δ, as a function of the median color excess, $E(B-V)$, for galaxies in the spec-z sample. Red triangles and blue squares are galaxies with strong Bayes-factor evidence toward SMC-like and starburst-like dust laws, respectively. Galaxies with low Bayes-factor evidence are shown as open white circles. For reference, a blue haze is shown where δ represents a starburst attenuation, where the width represents typical 1σ uncertainties on the posteriors of δ. Bottom: The joint probability between the δ and $E(B-V)$ posteriors. Medians in bins of $E(B-V)$ and their 68% limits are shown as salmon-colored points and error bars respectively. The spec-z sample suggests a relation between the scale of dust attenuation and the tilt of the dust law, such that galaxies with higher attenuation have a flatter (or gray) starburst-like dust law, and galaxies with relatively lower attenuation have a steeper, SMC-like dust law.

of Bayes-factor evidence on the IRX–β plane are the same for the phot-z sample.

Figure 10 shows that the phot-z sample of this work is able to reproduce the main result derived for the spec-z sample. In most cases, the Bayes-factor evidence promotes the same dust law as the observations suggest, based on their location in the IRX–β plane. However, there is significant scatter on the basis of individual galaxies, especially for the galaxies that seemingly promote an SMC92 attenuation (or discredit the starburst attenuation). This is to be expected; it is unlikely that all galaxies divide into two specific types of dust laws. For example, the SMC92-favored galaxies may have a range of attenuations that are, in different ways, steeper than the starburst dust law.

6.3.2. Fitting the Curve of the Dust Law: phot-z Sample

Figure 11 shows the Bayes-factor evidence of the galaxies in the phot-z sample as a function of their δ posterior median. The median tilt of the dust-attenuation curve, marginalized over all combinations of stellar population age, metallicity, and $E(B-V)$, agrees with the trends suggested by the Bayes-factor evidence. Galaxies with high SMC92 evidence tend to allocate their likelihood around steeper tilts to the attenuation law ($\delta < -0.2$), and galaxies with high starburst evidence allocate toward shallower tilts to the attenuation law ($\delta > 0$).

Figure 11 again shows that the results of the phot-z sample are an extension of the results from the spec-z sample (Figure 9). This figure shows that the steepness of the dust-attenuation curve correlates with the galaxy's attenuation optical depth, as parameterized by the color excess. Galaxies that seem to scatter away from the main trend have poor wavelength coverage of rest-frame UV wavelengths and have relatively broad posteriors in $E(B-V)$ and δ.

Figure 11 also shows the posterior joint probability between δ and $E(B-V)$ for all galaxies in the phot-z sample. In this depiction, the galaxies with poor constraints on δ or $E(B-V)$, which appear as outliers according to their median posteriors, get suppressed relative to the trend of the whole sample. The distribution shows a probability covariance such that galaxies with low attenuation optical depths have steeper dust laws and are well fit by the relation

$$\delta = (0.62 \pm 0.05)\log(E(B-V)) + 0.26 \pm 0.02. \quad (8)$$

We tested for the effect of the 2175 Å dust feature by refitting all the galaxies but excluding any band with a central

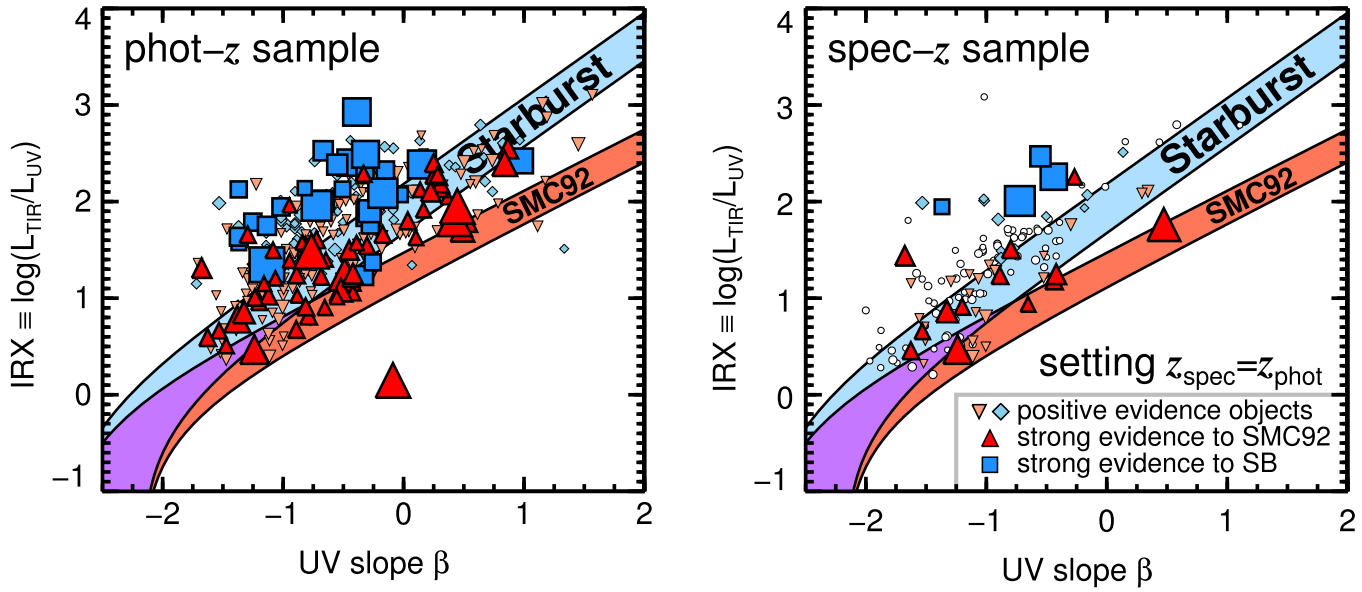

Figure 10. Left: The measured IR excesss vs. UV slope for the phot-z sample (see Section 2.3). For clarity, only galaxies with positive and strong Bayes-factor evidence are shown, with the symbol size scaling with the evidence. Curves show the predicted location of a variety of stellar populations according to an SMC92 or starburst dust-attenuation law. This panel shows that the galaxies in the phot-z sample selected by the strength of their Bayes-factor evidence follow the curve of their predicted dust-attenuation law with some scatter. Right: The same as the right panel of Figure 7 (galaxies from the spec-z sample), but with β and the Bayes-factor evidence recalculated when the photometric redshift is used for the spec-z sample. This panel shows that the selection methods and Bayes-factor evidence can overcome the errors from photometric-redshift estimates to predict galaxy dust laws, verified by their position in the IRX–β plane.

rest-frame wavelength within ± 250 Å of this feature. This excludes at most one band for each galaxy. The relation in Figure 11 was unchanged, implying that the dust feature does not affect our results.

7. DISCUSSION

7.1. Origins of the Relation Between $E(B-V)$ and δ

The parameter δ applies a spectral tilt to the attenuation law that pivots about the central wavelength of the V band. Unlike the original definition by Noll et al. (2009), our parameterization allows the total-to-selective attenuation at the V band, R_V, to change. This is because R_V is inversely proportional to the slope of the dust law around $\lambda = \lambda_V$, which means that low δ implies low R_V. This is physically motivated by the fact that different dust laws have different R_V. For example, $R_V = 2.95$ for the SMC dust law (Pei 1992) and $R_V = 4.05$ for the starburst dust law (Calzetti et al. 2000). Therefore, while the relation of Figure 11 displays a correlation between δ and $E(B-V)$, it could be interpreted as a correlation between R_V and $E(B-V)$. Intriguingly, this result may be the consequence of dust physics in galaxies. The value of R_V has been linked to the average dust grain size (Gordon et al. 2000), with smaller grains being associated with smaller R_V. However, even if the result in Figure 11 were linked to a change in dust grain size, it would still be difficult to comment on the dust production sources, given the short timescale for evolution of dust grains (Jones et al. 2013).

While there is some covariance between δ and $E(B-V)$ in the posteriors from the model fits, this does not drive the observed correlation between them. The covariance between the parameters can be understood as follows. Imagine an SED well represented by some δ and then apply a very small increase in δ toward a flatter dust curve, keeping other parameters fixed. This would produce less attenuation to UV bands, and the models respond by applying more likelihood to higher values of $E(B-V)$ in order to attenuate the UV. While this is a known parameter degeneracy that is unavoidable with the current data set, we explore a variety of tests in Appendix A to confirm that the relation in Figure 11 is real despite the influence of covariance. In addition, Figure 7 serves as independent, observational confirmation that the tilt of the dust law correlates with the amount of attenuation.

7.2. Physical Origins of Non-universal Attenuation

The ways in which dust grain type, size, and distribution affect the observed UV-to-NIR attenuation are enigmatic. There are many physically motivated explanations for how the relationship between stellar emission and the scattering and absorption by dust are manifest to an observed attenuation (Witt & Gordon 2000). One possible explanation for the change in observed attenuation for different galaxies is their orientation. There is evidence that galaxy inclination correlates with the strength of Lyα emission, such that we observe a smaller equivalent width of Lyα for more edge-on galaxies (Charlot & Fall 1993; Laursen & Sommer-Larsen 2007; Verhamme et al. 2012; Yajima et al. 2012; U et al. 2015). Resonant scattering and absorption by dust are likely the primary impediments to the escape of UV light from star-forming regions, and were predicted by Charlot & Fall (1993) to be exacerbated in edge-on galaxies. This agrees qualitatively with radiative transfer simulations that show an increasing attenuation optical depth with galaxy inclination (Chevallard et al. 2013). Therefore, based on physical models, one expects that galaxies with "grayer" dust laws and larger overall attenuation should have higher inclinations, on average.

However, we find no correlation with the scale or shape of attenuation and the axis ratios in either the phot-z or spec-z sample. Figure 12 shows the selection of galaxies in the phot-z sample with strong Bayes-factor evidence. The inset image stamps are a few examples that show similar morphologies

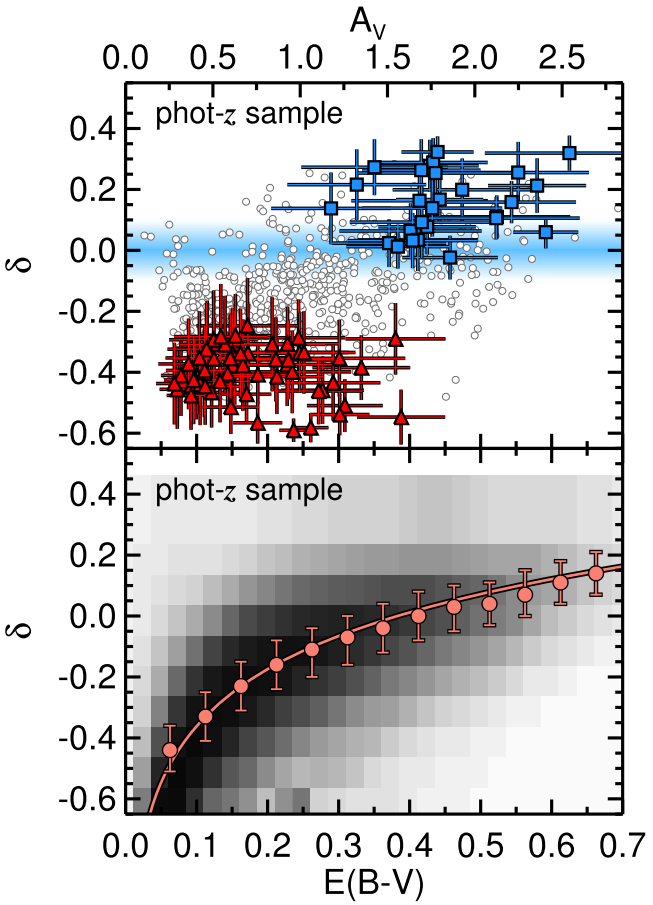

Figure 11. Same as Figure 9 but for the phot-z sample. Top: The medians of the δ and $E(B-V)$ posteriors are shown as gray circles, with galaxies that have strong Bayes-factor evidence highlighted as red triangles (SMC92-like) and blue squares (starburst-like). For reference, a blue haze is shown where δ represents a starburst attenuation, given typical uncertainties in δ. Bottom: The joint probability between the δ and $E(B-V)$ posteriors. The salmon-colored circles show δ at median likelihood in bins of $E(B-V)$, and error bars represent their 68% range in likelihood. The solid line represents a fit to the medians following Equation (8).

among SMC92-like and starburst-like galaxies. Compact red and clumpy extended galaxies with large axis ratio are found in both samples. A more detailed study with a wider mass range may be needed to find correlations with inclination, axis ratio, or Sérsic index. Alternatively, it may be that neither *HST* nor *Spitzer* provides wavelength coverage with high enough angular resolution to discern the trends between attenuation and morphology. Future observations with *James Webb Space Telescope* (with an angular resolution seven times higher than *Spitzer* at similar wavelengths) may be needed to offer spatial insight into the morphology of warm dust regions.

Even if galaxy orientation/inclination correlates with the strength of attenuation, it may not be the fundamental cause of non-universal shapes of the dust-attenuation law. For example, Chevallard et al. (2013) predicted the relation between δ and attenuation optical depth at all orientations, assuming only Milky Way-type dust grains. Their model predicted a relationship between the shape of the extinction law (here parameterized by δ) and the dust-attenuation optical depth. We consider this relationship in two scenarios: small and large dust-attenuation optical depths, τ, where the optical depth is related to the color excess by $\tau_\lambda = 0.92\, k_\lambda\, E(B-V)$.

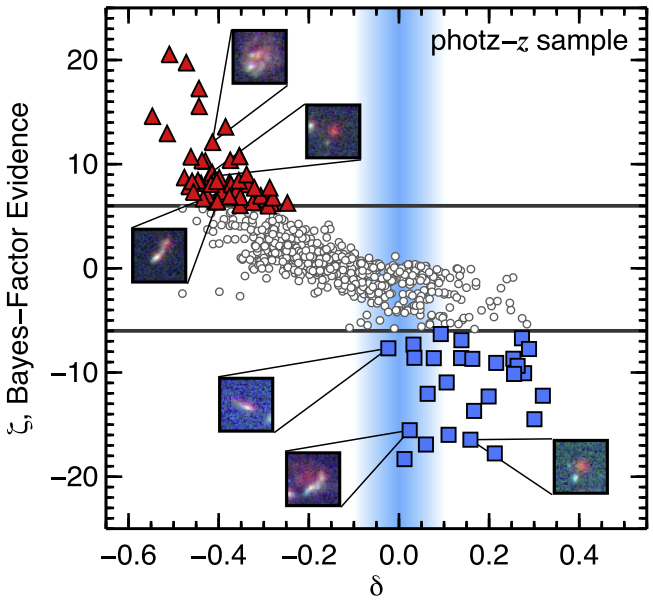

Figure 12. Top: Bayes-factor evidence vs. δ for the phot-z sample. Galaxies with strong Bayes-factor evidence are highlighted as red triangles (SMC92-like) and blue squares (starburst-like). Example RGB image stamps (H_{160}, V_{606}, and B_{435}) of galaxies from both subsamples are shown as insets. This figure demonstrates that there are no distinct morphological trends with δ or Bayes-factor evidence.

In the low-attenuation scenario, the steep curve of the dust law is likely a product of dust scattering, specifically the asymmetry parameter of the scattering phase function and its dependence on wavelength. The asymmetry parameter, g_λ, describes the degree of scattering in the forward direction (Mann et al. 2009). Dust is more forward-scattering at UV wavelengths, such that g_λ approaches unity, and more isotropic at optical-to-IR wavelengths, such that g_λ approaches zero (Gordon et al. 1994; Witt & Gordon 2000; Draine 2003). This means that in the regime of small optical depth, red light will tend to scatter isotropically and escape the galaxy, while blue light will tend to forward-scatter until absorption. Therefore, relatively more optical-to-IR light and less UV light escapes the galaxy, resulting in a steepening of the curve of dust attenuation ($\delta < 0$). This applies only at small optical depths where light has a chance to scatter out of the galaxy before absorption. Also in the low-attenuation scenario, dust is more transparent and scattering is less frequent, so the scattering asymmetry parameter may not be the only source of a steeper dust law. Galaxies with smaller dust optical depths may have steeper dust laws because they produce less scattering into the line of sight, causing the galaxy's dust-attenuation law to appear more like a dust-extinction law. In that case, the effects of dust grain size become more pronounced. For example, the steepness of the extinction law in the SMC has been attributed to its observed underabundance of carbon, which implies fewer heavy-element graphite grains than smaller silicate interstellar grains (Prevot et al. 1984). This picture is consistent with the trend of finding galaxies with more SMC-like dust at very high redshifts (e.g., $z > 5$ by Capak et al. 2015), where the metallicity of galaxies, in a broad sense, is expected to be lower (Madau & Dickinson 2014). The low δ for small $E(B-V)$ in this work can, at least in part, be attributed to lower R_V. Thus, the relation between $E(B-V)$ and δ could be a product of underlying relations in grain size, averaged over the surface brightness of the galaxy.

In the regime of large attenuation optical depths, attenuation becomes ubiquitous with wavelength. The flatter curve of the dust-attenuation law resulting from high attenuation is consistent with the picture proposed by Charlot & Fall (2000) whereby galaxies have a mixed distribution of stars and dust. In this case, any escaping UV light must come from regions of small optical depth, and will correspond to UV light at the outer "skin" of the mixed distribution (Calzetti 2001). Conversely, redder light will come from deeper physical locations within the region. The resulting attenuation function is gray, or flatter with wavelength, which translates to $\delta \geqslant 0$.

7.3. Comparison with Dust Theory

Figure 13 shows the predictions from radiative transfer calculations by Witt & Gordon (2000). In general, the curves of dust attenuation become grayer at increasing optical depths for models assuming SMC-like dust grains, a clumpy density distribution, and a spherical shell geometry. We determined δ for each curve using the definition in Equation (7) and compared its evolution with $E(B-V)$ to the results of Figure 11. The steepest curves in Figure 13 are poorly represented by the δ parameterization (their curvature is higher than a power law can reproduce), which explains the disagreement between $E(B-V)$ and δ at the low end. The radiative transfer relations at high and low optical depths are consistent with the observed correlation between $E(B-V)$ and δ found in this work.

Although the agreement in Figure 13 seems obvious given the prevalent predictions of dust theory (Bruzual et al. 1988; Witt et al. 1992; Charlot & Fall 2000; Gordon et al. 2001), radiative transfer simulations (Gordon et al. 2000; Witt & Gordon 2000; Chevallard et al. 2013), and observations of local nebular regions (Draine & Li 2001; Draine 2003), this is the first time the trend has been found from only UV-to-NIR broadband photometry of distant galaxies. Indeed, investigating origins of the relation between $E(B-V)$ and δ elucidates provocative explanations, as a result of similar correlations in stellar population age, metallicity, and dust grain size from dust theory.

7.4. Comparisons with Recent Literature

Several studies have noted populations of galaxies that lie off the nominal IRX–β relation of Meurer et al. (1999), suggesting that younger galaxies have steeper, SMC-like dust laws (Reddy et al. 2006, 2010, 2012; Siana et al. 2009; Buat et al. 2012; Sklias et al. 2014). Other recent studies find that galaxies at high redshift harbor dust laws that, at least in large subsets of their samples, agree with the assumption of a starburst dust law (Kriek & Conroy 2013; de Barros et al. 2015; Scoville et al. 2015; Zeimann et al. 2015). Our results suggest that these studies are not in conflict but provide clues to the overall non-universality of how dust attenuates light in star-forming galaxies. For example, the studies that find evidence for starburst-like dust laws do so with galaxies selected by their strong nebular emission lines (e.g., Hα and Hβ), by recent star formation activity (strong C IV absorption), and/or by SEDs with appreciable reddening, allowing the underlying dust law to be tested. A common thread to these starburst-dust galaxies is their large dust-attenuation optical depths, assuming that galaxies with strong nebular features also have high levels of stellar attenuation by dust, averaged over the whole galaxy as a foreground screen (see Penner et al. 2015 for a discussion on alternatives to the foreground screen).

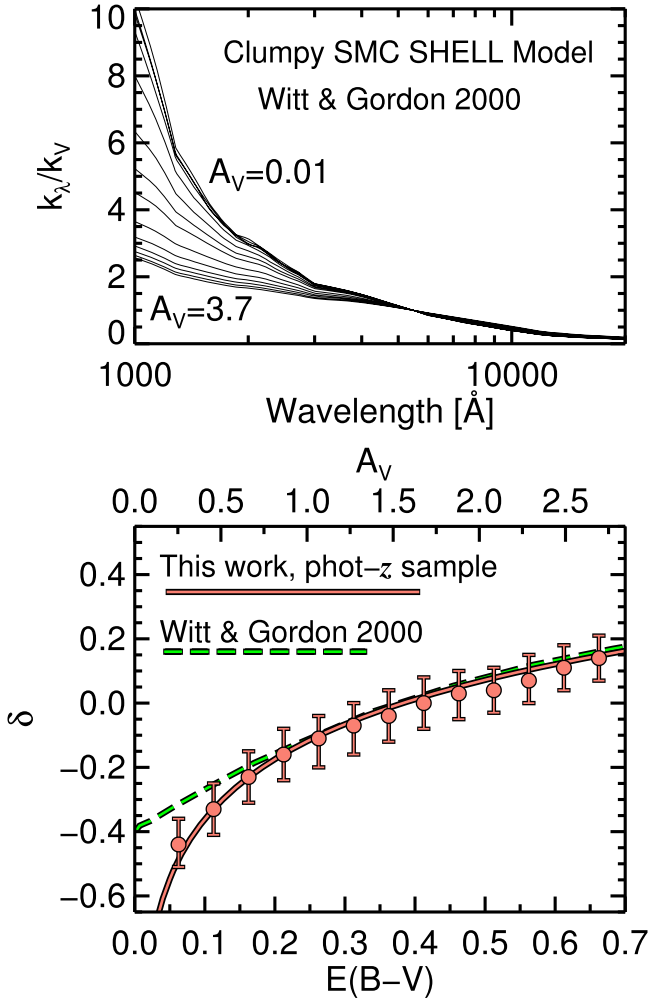

Figure 13. Top: Attenuation curves from the radiative transfer calculations by Witt & Gordon (2000) assuming SMC-like dust grains, a clumpy density distribution, and a spherical shell geometry. Bottom: The relation between $E(B-V)$ and δ from Figure 11. The salmon-colored circles show δ at median likelihood in bins of $E(B-V)$, and error bars represent their 68% range in likelihood. The solid line represents a fit to the medians following Equation (8). The dashed green line represents radiative transfer predictions from the above dust-attenuation models.

The trend with δ and $E(B-V)$ (or with IRX) was also found by Buat et al. (2012) and Kriek & Conroy (2013). The latter authors attributed the change in δ to a change in the strength of the equivalent width of Hα. The difference in this study is that the evolution of δ is determined for individual galaxies based on rest-frame UV-to-NIR broadband photometry, suggesting that the methods can be used at even higher redshifts.

7.5. Implications for SED-derived Properties of Galaxies

The determination that individual galaxies at $z \sim 2$ have different dust laws has several implications for determinations of the evolution of distant galaxies. At relatively low $E(B-V)$ ($\approx$0.1), this is manifest as an underprediction by a factor of $\approx$2 in the dust correction to the 1500 Å luminosity ($10^{0.4k_\lambda E(B-V)}$) and therefore UV SFR compared to the assumption of a $\delta = 0$ starburst. Higher SFRs for SMC92-like galaxies agree with the determination of stellar population ages: galaxies with an SMC92-like attenuation are on average half the age of galaxies with a starburst-like attenuation, consistent with the results of previous studies (Siana et al. 2009; Reddy et al. 2010). At

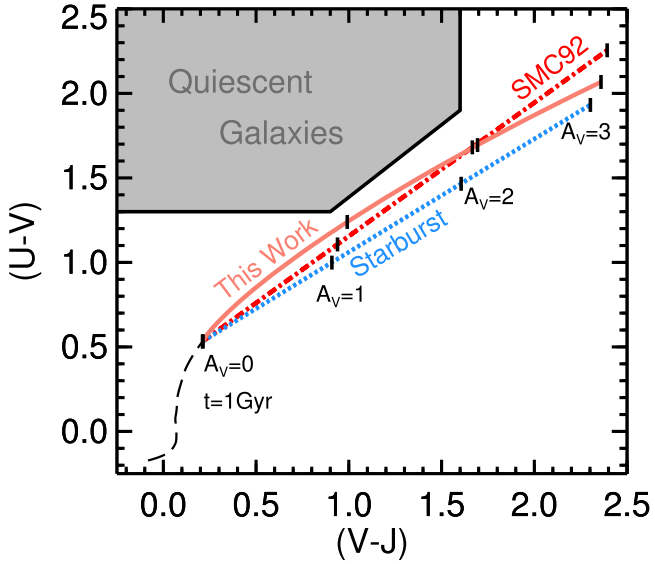

Figure 14. Tracks of dust attenuation under different dust laws on the *UVJ* diagram. The dashed black line follows the age of a stellar population with a constant star formation history from $t = 0.02$ Gyr to $t = 1$ Gyr. The colored lines show how the rest-frame *UVJ* colors of the $t = 1$ Gyr stellar population change with increasing levels of attenuation ($0 < A_V < 3$) following a starburst-like dust law (blue, dotted), an SMC92-like dust law (red, dotted–dashed), and a dust law that follows Equation (8) (salmon, solid).

$E(B-V) > 0.6$, dust corrections to the UV luminosity are overestimated by a factor of 2–5 compared to the starburst-dust assumption at fixed $E(B-V)$.

The dust law also has implications for studies that use the rest-frame colors to infer dust attenuation in star-forming galaxies. The rest-frame *UVJ* diagram is a particularly helpful visualization used to break the degeneracy between old stellar population ages and reddening due to dust (Wuyts et al. 2007; Williams et al. 2009). Star-forming galaxies move along the *UVJ* diagram in an identifiable relation, where the redder colors relate to increasing levels of attenuation by dust (Price et al. 2014; J. Fang et al. 2016, in preparation; Forrest et al. 2016). Figure 14 shows how the rest-frame *UVJ* colors change with attenuation under different assumed dust laws. The dust law derived in this work may induce slight differences in the positions of star-forming galaxies, but these will be degenerate with SFHs and age/metallicity variations. In addition, the dust law would not significantly influence the selection between star-forming and quiescent galaxies.

Lastly, the relationship between δ and $E(B-V)$ does not translate to a relationship between the UV spectral slope β and the dust law. At fixed β there is high scatter in IRX (see Figures 7 and 10). Even at relatively modest UV slopes, $-1 < \beta < 0$, the scatter in $L_{\rm TIR}/L_{\rm UV}$ is more than 1 dex depending on the assumption of the dust attenuation law (Buat et al. 2012). This may have a substantive impact on the interpretation of the intrinsic UV luminosity function if the dust corrections to the observed UV luminosity densities assume a unique relationship between $M_{\rm UV}$ and β.

8. CONCLUSIONS

We investigate the shape of the dust-attenuation law in star-forming galaxies at $z \sim 2$ in the CANDELS GOODS-N and GOODS-S deep fields. We apply a Bayesian SED-fitting technique to galaxies with spectroscopic and photometric redshifts, and determine the evidence for their underlying dust law and its correlation with other physical properties of the galaxies. Our results can be summarized as follows:

1. IR-luminous galaxies at $z \sim 2$ can be characterized by a range of dust laws bounded by two types: (1) a starburst-like (Calzetti et al. 2000) attenuation that is grayer (flatter) across UV-to-NIR wavelengths and (2) a dust law that steepens toward the rest-frame FUV like the curve of the SMC extinction law (Pei 1992).
2. The dust law inferred from rest-frame UV-to-NIR photometry of galaxies is supported by their position along the IRX–β relations. This result gives credibility that a Bayesian analysis of rest-frame UV-to-NIR fluxes is capable of broadly distinguishing between dust laws that are gray or steep in the rest-frame FUV.
3. The steepness of the dust law, parameterized by a δ power-law deviation from the starburst dust law, is correlated with their color excess, $E(B-V)$, for IR-bright galaxies at $z \sim 2$. Galaxies with lower levels of dust attenuation have dust laws that are steeper in the rest-frame FUV, following $\delta = (0.62 \pm 0.05)\log(E(B-V)) + 0.26 \pm 0.02$.
4. The relation between $E(B-V)$ and δ is further supported by predictions from radiative transfer. The agreement with dust theory offers possible interpretations for the relation and its origins from different dust production mechanisms. For example, the change in the shape of the dust law may be a result of star–dust geometry, properties of dust grains, and/or stellar population age, emphasizing the non-universality of the dust law in star-forming galaxies.

We thank the referee for thoughtful and constructive feedback on this work. We acknowledge our colleagues in the CANDELS collaboration for very useful comments and suggestions. We also thank the great effort of all the CANDELS team members for their work to provide a robust and valuable data set. We thank Karl Gordon for insightful discussions on the physical implications of these results. We also thank Daniela Calzetti and Veronique Buat for helpful comments and comments. This work is based in part on observations taken by the CANDELS Multi-Cycle Treasury Program with the NASA/ESA *HST*, which is operated by the Association of Universities for Research in Astronomy, Inc., under NASA contract NAS5-26555. This work is supported by *HST* program No. GO-12060. Support for Program No. GO-12060 was provided by NASA through a grant from the Space Telescope Science Institute, which is operated by the Association of Universities for Research in Astronomy, Incorporated, under NASA contract NAS5-26555. We acknowledge the Spanish MINECO grant AYA2012-31277 for funding the contribution from Pablo Pérez-González. This work is based in part on observations made with the *Spitzer Space Telescope*, which is operated by the Jet Propulsion Laboratory, California Institute of Technology under contract with the National Aeronautics and Space Administration (NASA). The authors acknowledge the Texas A&M University Brazos HPC cluster that contributed to the research reported here. URL: http://brazos.tamu.edu.

APPENDIX A
TESTING THE RELATIONSHIP BETWEEN $E(B-V)$ AND δ

The main result of this paper is the relationship between the tilt of the dust law δ and the amount of attenuation as probed by

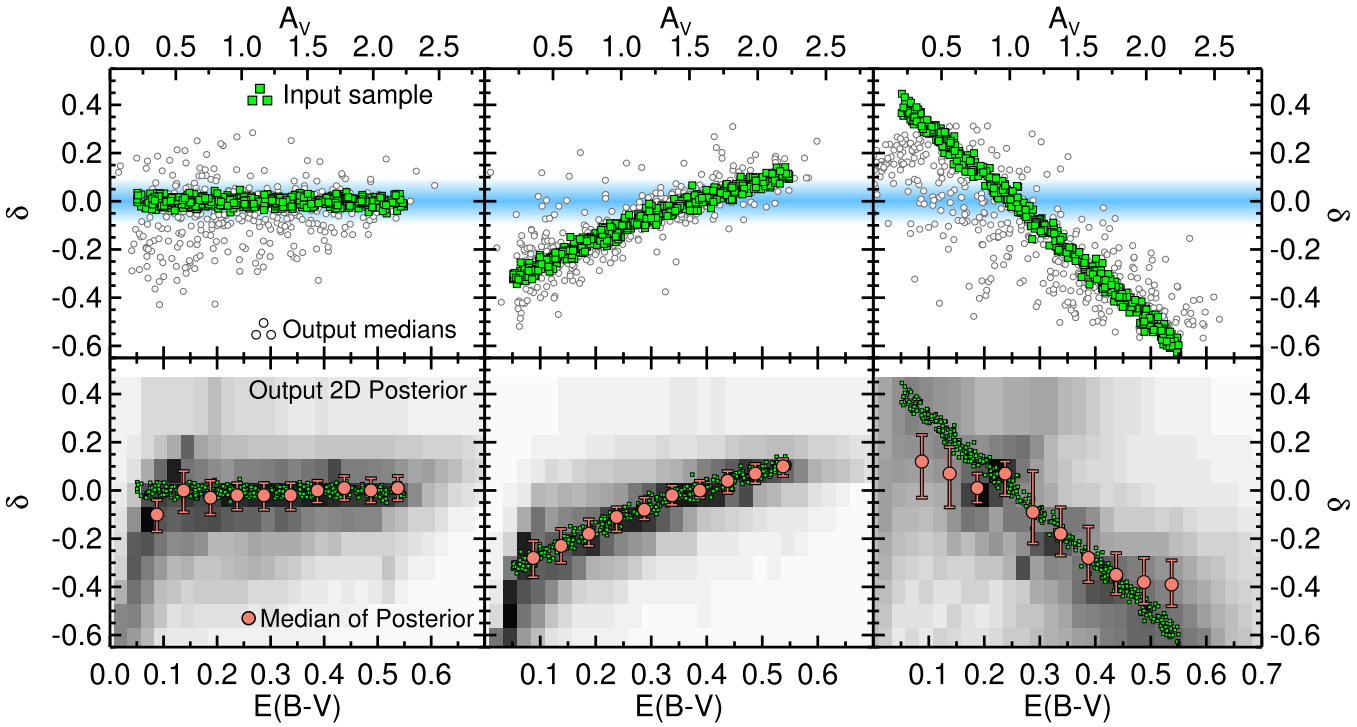

Figure 15. Tilt of the dust-attenuation curve, δ, as a function of $E(B-V)$ for several input test samples to examine the robustness of the main relation in Figure 11. Green squares represent the input $E(B-V)$ and δ with a known model SED. The left panels show a model where delta is constant with $E(B-V)$, the right panels show a model where delta declines with $E(B-V)$, and the middle panel shows a model with the relation from Witt & Gordon (2000) (shown in Figure 13). The model fluxes are perturbed and assigned uncertainty according to the real errors in the data. The recovered median values of each δ and $E(B-V)$ posterior are shown as gray circles (top). The combined two-dimensional posterior for the whole input sample is shown in the lower panels, where shaded regions represent higher likelihood for the sample, salmon-colored circles show δ at median likelihood in bins of $E(B-V)$, and error bars represent their 68% range in likelihood.

the color excess, $E(B-V)$. While this relationship is qualtitatively and independently supported by the position of galaxies on the IRX–β relation and their Bayes-factor evidence, it is prudent to consider whether the covariance between δ and $E(B-V)$ contributes to the observed correlation (Figure 11). We addressed this concern with several tests below.

First, we defined a grid of δ and $E(B-V)$ that spans the plane in Figure 11. Then, we calculated fluxes from our model SEDs for each value of δ and $E(B-V)$. The model flux at each bandpass was perturbed according to a Gaussian error distribution where sigma was defined as the average, flux-dependent signal-to-noise ratio of the CANDELS data. We used those fluxes as inputs to our procedure and compared the derived values to the "true" values of δ and $E(B-V)$. We repeated this test 15 times for five assumptions of the stellar population age of the input SED and three assumptions of metallicity.

We find that when the input stellar population age is less than 1 Gyr, we accurately recover all "true" δ and $E(B-V)$ with no systematics or appreciable covariance and for all input metallicities. The covariance begins to appear when the galaxies are older than 1 Gyr, and the effect increases in strength at higher metallicities. In that case, the posterior distributions for $E(B-V)$ and δ are systematically shifted by ~20% of their respective input values, where the covariance is positive and moves models with higher δ to higher $E(B-V)$ and vice versa.

The results of the above test are unsurprising. Redder intrinsic SEDs will be fainter in the rest-frame UV, and by construction, the fainter model fluxes are assigned higher uncertainties. Older ages redden an SED in a similar manner to having high $E(B-V)$ and high δ or low $E(B-V)$ and low δ, especially when uncertainties in the rest-frame UV are high. This causes a broadening in the posteriors of both δ and $E(B-V)$ in a way that is correlated, causing a covariance.

Second, we then asked whether the distribution of galaxy ages in our sample is low enough such that the covariance does not significantly bias the relation between $E(B-V)$ and δ. We addressed this with a similar test, where we fixed the age distribution of galaxies to be the same as the one we measure for the GOODS-S phot-z sample. The input $E(B-V)$ was assigned to a random value, and the input δ follows one of three test relationships: δ is constant with $E(B-V)$, δ increases with $E(B-V)$, and δ decreases with $E(B-V)$. For the case of increasing δ, we used the relationship from Witt & Gordon (2000) (shown in Figure 13) as the input. The input δ values were also given a small random scatter to simulate a more realistic relation and uncertainty in δ.

We find that the input relation was well recovered for a sample similar to the phot-z sample of GOODS-S with a realistic input age distribution. Figure 15 summarizes the results of this final test. While the primary relation was recovered, the covariances conspire to recover the increasing-δ relation with less scatter and the decreasing-δ relation with more. In addition, at $E(B-V) \lesssim 0.1$ the attenuation is not strong enough to clearly distinguish between different dust laws. We conclude that (1) we are able to recover several types of relationships on the plane of Figure 11, and (2) there may be some bias at $E(B-V) \lesssim 0.1$, but because the attenuation is low regardless, the effect is small. At $E(B-V) = 0.05$, the uncertainty of $\Delta(\delta) = 0.1$ changes the attenuation at 1500 Å by only 10%. As supported by the observations in the IRX–β relation, this test gives credence to

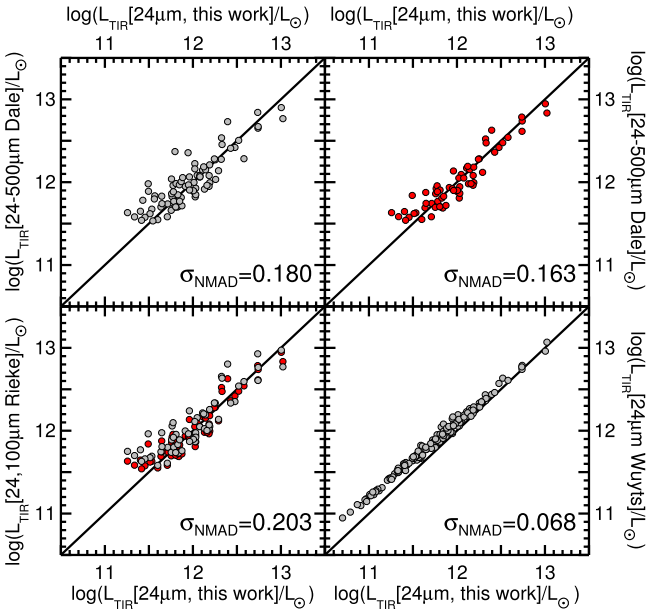

Figure 16. Galaxies in the spec-z sample with *Herschel* PACS and/or SPIRE detections are shown with several determinations of $L_{\rm TIR}$ as a function of the fiducial 24 μm method. The top panels assume fitting templates of Dale & Helou (2002) for all available FIR detections (top left) or 24 and 100 μm only (top right). The bottom left panel assumes templates of Rieke et al. (2009) for 24 and 100 μm bands (gray), as well the assumption of Dale et al. (red). The bottom right panel uses the 24 μm conversion to $L_{\rm TIR}$ from Wuyts et al. (2008).

the belief that the relation in Figure 11 is real and not an artifact of the SED-fitting procedure.

APPENDIX B
USING *HERSCHEL* TO CALCULATE THE TOTAL INFRARED LUMINOSITIES

The determinations of $L_{\rm TIR}$ used in this work come from conversions of 24 μm luminosity calibrated by R13. However, ≈40% of our sample have detections at longer wavelengths with *Herschel*, providing the opportunity to internally test our $L_{\rm TIR}$ measurements. We determined $L_{\rm TIR}$ by fitting several different suites of FIR SED templates to the observed MIPS 24 μm and/or *Herschel* PACS and SPIRE detections of galaxies in our spec-z sample.

Figure 16 shows several $L_{\rm TIR}$ calculations compared to our fiducial $L_{\rm TIR}$ determined from the 24 μm luminosity. We compared our adopted $L_{\rm TIR}$ with $L_{\rm TIR}$ values derived from fitting the full IR SED to templates of Dale & Helou (2002) and Rieke et al. (2009), as well as fitting to fluxes at 24−100 μm only. In addition, we compare the 24 μm conversion to $L_{\rm TIR}$ proposed by Wuyts et al. (2008, 2011a, 2011b). The R13 calibration is very similar to that by Wuyts et al. In all cases, the scatter in the derived $L_{\rm TIR}$ is within $\sigma_{\rm NMAD} \approx 0.2$ dex. This scatter is smaller than the correlations in IRX–β found in our primary results, and therefore our approximation of 24 μm luminosity to $L_{\rm TIR}$ is reasonable.

One benefit to using the 24 μm flux to estimate $L_{\rm TIR}$ is that longer-wavelength data, such as >70–160 μm, could be affected more by the heating of cold dust from old stars. Other studies have shown that the longer-wavelength data show more scatter in the SFR calibration for this reason (see Kennicutt et al. 2009; Rieke et al. 2009). In any case, this is likely not a significant factor in our sample (for example, dust heating from old stellar

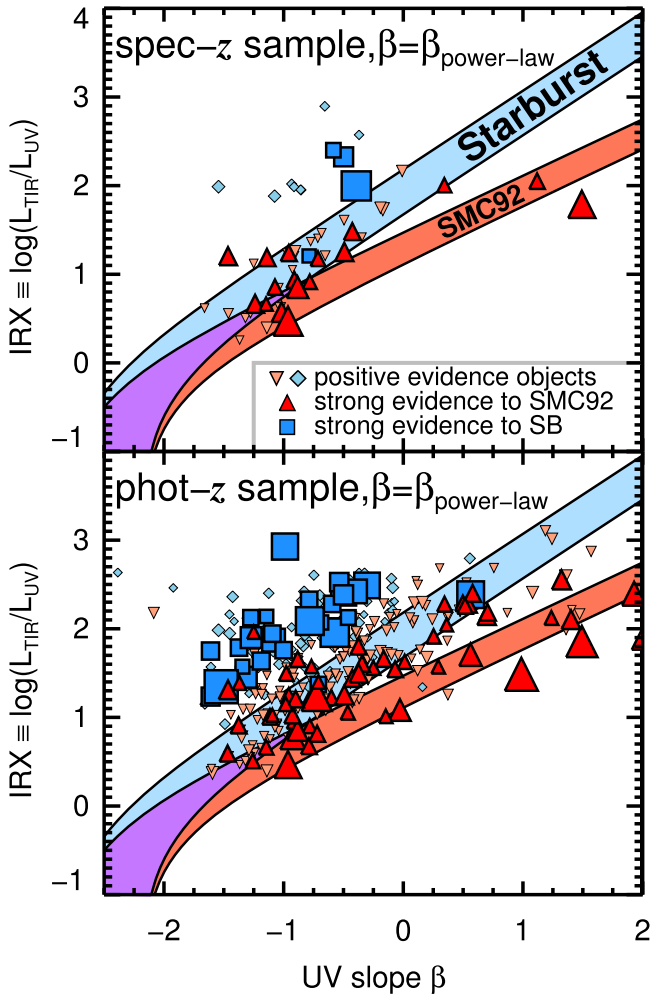

Figure 17. IRX–β relation for the spec-z (top) and phot-z (bottom) samples, where β was derived from a power-law fit to the observed rest-frame UV fluxes.

populations, which can lead to increased scatter, is mostly important for lower-luminosity galaxies, and accounts for <10% of the total IR luminosity for $L_{\rm TIR} > 10^{11}$ $L_\odot$ (Bell 2002; Calzetti et al. 2010)). For these reasons the 24 μm calibration of R13 (and others in the literature) should be valid with a scatter of ∼0.2 dex. Lastly, we point out that any uncertainty from the $L_{\rm TIR}$ calibration affects only the discussion of the IRX–β relation and not the derivation of the relation between $E(B-V)$ and δ, which is based on the modeling of the UV-to-near-IR SED and is independent of the total IR luminosities.

APPENDIX C
CHANGING THE UV SLOPE, β

As described in Section 2.7, we ran tests to recover the true β when calculating β from a power-law fit to the UV or when using the best-fit SED. For our data, the best-fit SED technique of Finkelstein et al. (2012) reproduced the input β, while the power-law method produced some systematics that worsened at higher redshifts. Figure 17 shows how the results of Figures 7 and 10 would change when β is calculated from a power-law fit to the observed UV bands. For both the spec-z and phot-z samples, the position of galaxies on IRX–β broadly agrees with the favored dust law according to the Bayes-factor evidence, in some cases more than the fiducial plots. Importantly, small

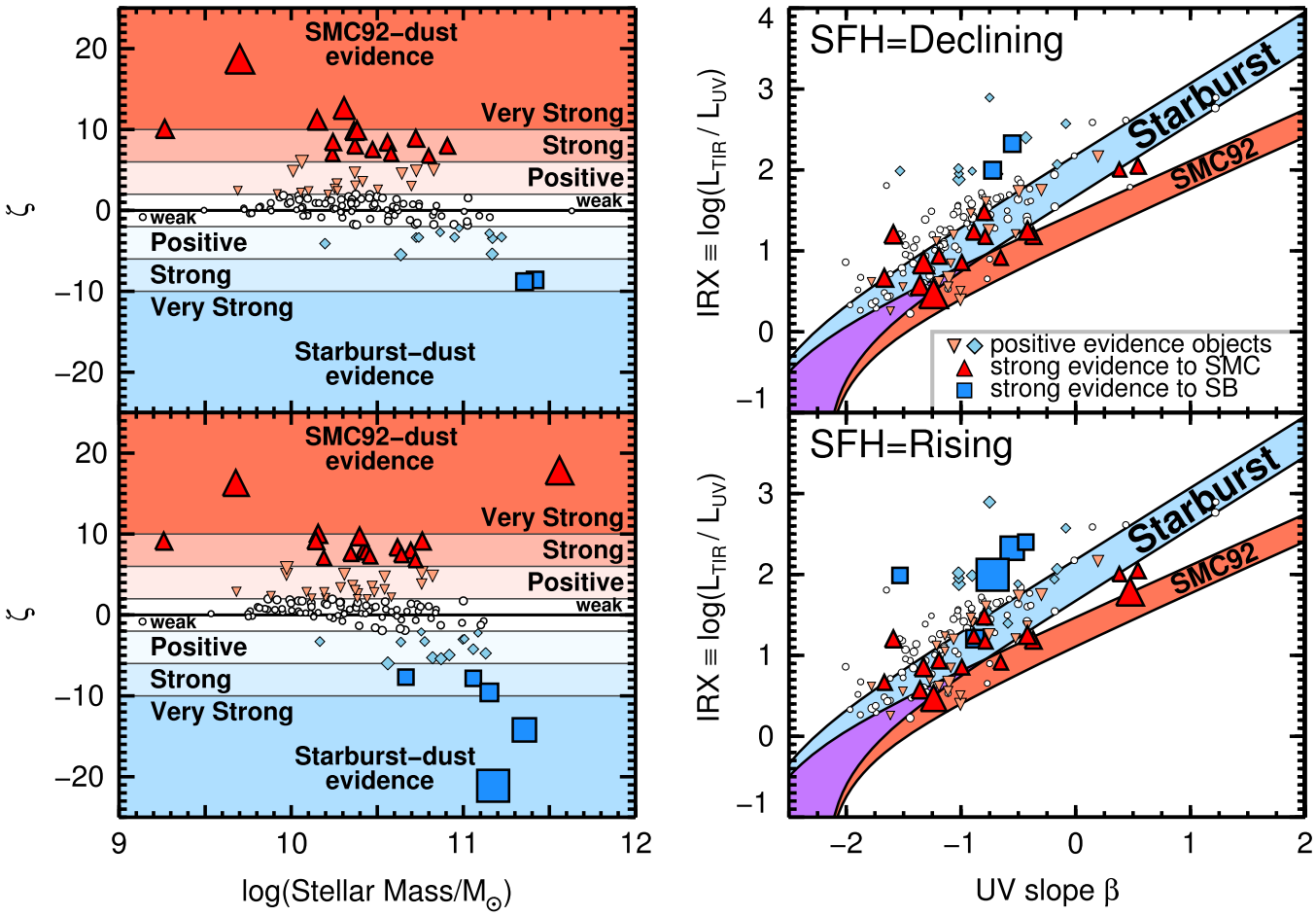

Figure 18. Same as Figure 7, but allowing the star formation history to vary as a fitted parameter for star formation rates that decline (top) and rise (bottom) with time. Several colored tiers indicate the selection of galaxies to have strong Bayes-factor evidence toward an SMC92 (red triangles) or starburst (blue squares) dust law. Although the strength of evidence shifts when allowing the SFH to be free, galaxies only ever lose or gain in their favor toward a single dust law; no galaxy changes the direction of its evidence.

changes in β do not change the clear divide in IRX between galaxies with opposing levels of Bayes-factor evidence. For example, galaxies with evidence promoting a starburst-like dust law tend to have higher IRX than those promoting an SMC-like dust law, at any given β. This provides evidence that the method is correctly identifying galaxies with opposing dust laws.

APPENDIX D
CHANGING THE ASSUMED SFH

For the primary results of this work, we used stellar population models that assume a constant SFH. However, we must consider whether our choice of parameter space is missing models that could mimic the SED-fitting evidence toward certain dust laws. In this appendix, we allow the *e*-folding timescale (τ), the time interval over which the SFR is increased by a factor of *e*, to vary as a parameter. We consider SFRs that rise and decline with cosmic time with ranges described in Table 1. We also include the fits to rising histories in Figures 5 and 6 to illustrate that the additional parameter does not create SED shapes that mimic the evidence toward different dust laws.

Figure 18 shows how fitting the spec-*z* sample with a range of SFHs affects the selection of galaxies based on their Bayes-factor evidence and how that selection propagates to the IRX–β plane. While the distribution of Bayes-factor evidence shifts under the influence of a new parameter, there are still galaxies with convincing evidence between dust laws. In addition, no galaxy switches evidence from favoring the SMC92-like dust to favoring starburst-like dust or vice versa. We conclude that the evidence between dust laws is not an artifact of different SFHs, at least for simple rising and declining τ-models.

REFERENCES

Ashby, M. L. N., Willner, S. P., Fazio, G. G., et al. 2013, ApJ, 769, 80
Balestra, I., Mainieri, V., Popesso, P., et al. 2010, A&A, 512, A12
Beckwith, S. V. W., Stiavelli, M., Koekemoer, A. M., et al. 2006, AJ, 132, 1729
Bell, E. F. 2002, ApJ, 577, 150
Boquien, M., Buat, V., Boselli, A., et al. 2012, A&A, 539, A145
Boquien, M., Calzetti, D., Kennicutt, R., et al. 2009, ApJ, 706, 553
Brammer, G. B., van Dokkum, P. G., & Coppi, P. 2008, ApJ, 686, 1503
Bruzual, G., & Charlot, S. 2003, MNRAS, 344, 1000
Bruzual, G., Magris, G., & Calvet, N. 1988, ApJ, 333, 673
Buat, V., Giovannoli, E., Burgarella, D., et al. 2010, MNRAS, 409, L1
Buat, V., Giovannoli, E., Heinis, S., et al. 2011, A&A, 533, A93
Buat, V., Iglesias-Páramo, J., Seibert, M., et al. 2005, ApJL, 619, L51
Buat, V., Noll, S., Burgarella, D., et al. 2012, A&A, 545, A141
Burgarella, D., Buat, V., & Iglesias-Páramo, J. 2005, MNRAS, 360, 1413
Calzetti, D. 1997, in AIP Conf. Ser. 408, The Ultraviolet Universe at Low and High Redshift, ed. W. H. Waller (Melville, NY: AIP), 403
Calzetti, D. 2001, PASP, 113, 1449
Calzetti, D., Armus, L., Bohlin, R. C., et al. 2000, ApJ, 533, 682
Calzetti, D., Kinney, A. L., & Storchi-Bergmann, T. 1994, ApJ, 429, 582
Calzetti, D., Wu, S.-Y., Hong, S., et al. 2010, ApJ, 714, 1256

Capak, P. L., Carilli, C., Jones, G., et al. 2015, Natur, 522, 455
Casey, C. M., Narayanan, D., & Cooray, A. 2014a, PhR, 541, 45
Casey, C. M., Scoville, N. Z., Sanders, D. B., et al. 2014b, ApJ, 796, 95
Charlot, S., & Fall, S. M. 1993, ApJ, 415, 580
Charlot, S., & Fall, S. M. 2000, ApJ, 539, 718
Chevallard, J., Charlot, S., Wandelt, B., & Wild, V. 2013, MNRAS, 432, 2061
Conroy, C., & Gunn, J. E. 2010, ApJ, 712, 833
Daddi, E., Dannerbauer, H., Stern, D., et al. 2009, ApJ, 694, 1517
Dahlen, T., Mobasher, B., Faber, S. M., et al. 2013, ApJ, 775, 93
Dale, D. A., & Helou, G. 2002, ApJ, 576, 159
Dale, D. A., Helou, G., Contursi, A., Silbermann, N. A., & Kolhatkar, S. 2001, ApJ, 549, 215
Davé, R., Finlator, K., & Oppenheimer, B. D. 2011, MNRAS, 416, 1354
de Barros, S., Reddy, N., & Shivaei, I. 2015, arXiv:1509.05055
Doherty, M., Bunker, A. J., Ellis, R. S., & McCarthy, P. J. 2005, MNRAS, 361, 525
Donley, J. L., Koekemoer, A. M., Brusa, M., et al. 2012, ApJ, 748, 142
Draine, B. T. 2003, ApJ, 598, 1017
Draine, B. T., & Li, A. 2001, ApJ, 551, 807
Elbaz, D., Dickinson, M., Hwang, H. S., et al. 2011, A&A, 533, A119
Elíasdóttir, Á, Fynbo, J. P. U., Hjorth, J., et al. 2009, ApJ, 697, 1725
Ellis, R. S., McLure, R. J., Dunlop, J. S., et al. 2013, ApJL, 763, L7
Fadda, D., Yan, L., Lagache, G., et al. 2010, ApJ, 719, 425
Finkelstein, S. L., Papovich, C., Salmon, B., et al. 2012, ApJ, 756, 164
Forrest, B., Tran, K.-V. H., Tomczak, A. R., et al. 2016, ApJL, 818, L26
Gall, C., Andersen, A. C., & Hjorth, J. 2011a, A&A, 528, A13
Gall, C., Andersen, A. C., & Hjorth, J. 2011b, A&A, 528, A14
Gall, C., Hjorth, J., & Andersen, A. C. 2011c, A&ARv, 19, 43
Giavalisco, M., Ferguson, H. C., Koekemoer, A. M., et al. 2004, ApJL, 600, L93
Gordon, K. D., Clayton, G. C., Misselt, K. A., Landolt, A. U., & Wolff, M. J. 2003, ApJ, 594, 279
Gordon, K. D., Clayton, G. C., Witt, A. N., & Misselt, K. A. 2000, ApJ, 533, 236
Gordon, K. D., Misselt, K. A., Witt, A. N., & Clayton, G. C. 2001, ApJ, 551, 269
Gordon, K. D., Witt, A. N., Carruthers, G. R., Christensen, S. A., & Dohne, B. C. 1994, ApJ, 432, 641
Grogin, N. A., Kocevski, D. D., Faber, S. M., et al. 2011, ApJS, 197, 35
Guo, Q., White, S., Boylan-Kolchin, M., et al. 2011, MNRAS, 413, 101
Guo, Y., Ferguson, H. C., Giavalisco, M., et al. 2013, ApJS, 207, 24
Heckerman, D. 1995, A Tutorial on Learning with Bayesian Networks, in Learning in Graphical Models (Cambridge, MA: MIT Press)
Illingworth, G. D., Magee, D., Oesch, P. A., et al. 2013, ApJS, 209, 6
Jeffreys, H. 1935, Journal of the Royal Statistical Society, 98, 39
Jeffreys, H. 1961, Theory of Probability (3rd ed.; Oxford: Oxford Univ. Press)
Jones, A. P., Fanciullo, L., Köhler, M., et al. 2013, A&A, 558, A62
Kass, R. E., & Raftery, A. E. 1995, J. Am. Stat. Assoc., 90, 773
Kennicutt, R. C., Jr. 1998, ARA&A, 36, 189
Kennicutt, R. C., Jr., Hao, C.-N., Calzetti, D., et al. 2009, ApJ, 703, 1672
Kinney, A. L., Calzetti, D., Bohlin, R. C., et al. 1996, ApJ, 467, 38
Koekemoer, A. M., Ellis, R. S., McLure, R. J., et al. 2013, ApJS, 209, 3
Koekemoer, A. M., Faber, S. M., Ferguson, H. C., et al. 2011, ApJS, 197, 36
Kriek, M., & Conroy, C. 2013, ApJL, 775, L16
Kriek, M., van Dokkum, P. G., Franx, M., et al. 2008, ApJ, 677, 219
Laidler, V. G., Papovich, C., Grogin, N. A., et al. 2007, PASP, 119, 1325
Laursen, P., & Sommer-Larsen, J. 2007, ApJL, 657, L69
Lee, K.-S., Dey, A., Reddy, N., et al. 2011, ApJ, 733, 99
Lee, S.-K., Ferguson, H. C., Somerville, R. S., Wiklind, T., & Giavalisco, M. 2010, ApJ, 725, 1644
Madau, P., & Dickinson, M. 2014, ARA&A, 52, 415
Mancuso, C., Lapi, A., Shi, J., et al. 2016, ApJ, 823, 128
Mann, I., Nakamura, A. M., & Mukai, T. (ed.) 2009, Small Bodies in Planetary Systems, Vol. 758 (Berlin: Springer)
Meiksin, A. 2006, MNRAS, 365, 807
Meurer, G. R., Heckman, T. M., & Calzetti, D. 1999, ApJ, 521, 64
Meurer, G. R., Heckman, T. M., Leitherer, C., et al. 1995, AJ, 110, 2665
Mignoli, M., Cimatti, A., Zamorani, G., et al. 2005, A&A, 437, 883
Mitchell, P. D., Lacey, C. G., Baugh, C. M., & Cole, S. 2013, MNRAS, 435, 87
Morgan, H. L., & Edmunds, M. G. 2003, MNRAS, 343, 427
Muñoz-Mateos, J. C., Gil de Paz, A., Boissier, S., et al. 2009, ApJ, 701, 1965
Nardini, E., Risaliti, G., Watabe, Y., Salvati, M., & Sani, E. 2010, MNRAS, 405, 2505
Newton, M. A., Czado, C., & Chappell, R. 1996, J. Am. Stat. Assoc., 91, 142
Noll, S., Pierini, D., Cimatti, A., et al. 2009, A&A, 499, 69
Noll, S., Pierini, D., Pannella, M., & Savaglio, S. 2007, A&A, 472, 455
Noterdaeme, P., Ledoux, C., Srianand, R., Petitjean, P., & Lopez, S. 2009, A&A, 503, 765
Nozawa, T., Asano, R. S., Hirashita, H., & Takeuchi, T. T. 2015, MNRAS, 447, L16
Nozawa, T., Kozasa, T., Umeda, H., Maeda, K., & Nomoto, K. 2003, ApJ, 598, 785
Overzier, R. A., Heckman, T. M., Wang, J., et al. 2011, ApJL, 726, L7
Pacifici, C., Charlot, S., Blaizot, J., & Brinchmann, J. 2012, MNRAS, 421, 2002
Padovani, P., Miller, N., Kellermann, K. I., et al. 2011, ApJ, 740, 20
Papovich, C., Dickinson, M., & Ferguson, H. C. 2001, ApJ, 559, 620
Papovich, C., Finkelstein, S. L., Ferguson, H. C., Lotz, J. M., & Giavalisco, M. 2011, MNRAS, 412, 1123
Papovich, C., Moustakas, L. A., Dickinson, M., et al. 2006, ApJ, 640, 92
Papovich, C., Rudnick, G., Le Floc'h, E., et al. 2007, ApJ, 668, 45
Pei, Y. C. 1992, ApJ, 395, 130
Penner, K., Dickinson, M., Weiner, B., et al. 2015, arXiv:1507.00728
Pforr, J., Maraston, C., & Tonini, C. 2012, MNRAS, 422, 3285
Pforr, J., Maraston, C., & Tonini, C. 2013, MNRAS, 435, 1389
Popesso, P., Dickinson, M., Nonino, M., et al. 2009, A&A, 494, 443
Prevot, M. L., Lequeux, J., Prevot, L., Maurice, E., & Rocca-Volmerange, B. 1984, A&A, 132, 389
Price, S. H., Kriek, M., Brammer, G. B., et al. 2014, ApJ, 788, 86
Reddy, N., Dickinson, M., Elbaz, D., et al. 2012, ApJ, 744, 154
Reddy, N. A., Erb, D. K., Pettini, M., Steidel, C. C., & Shapley, A. E. 2010, ApJ, 712, 1070
Reddy, N. A., Kriek, M., Shapley, A. E., et al. 2015, ApJ, 806, 259
Reddy, N. A., Steidel, C. C., Fadda, D., et al. 2006, ApJ, 644, 792
Rieke, G. H., Alonso-Herrero, A., Weiner, B. J., et al. 2009, ApJ, 692, 556
Rujopakarn, W., Rieke, G. H., Eisenstein, D. J., & Juneau, S. 2011, ApJ, 726, 93
Rujopakarn, W., Rieke, G. H., Weiner, B. J., et al. 2013, ApJ, 767, 73
Salmon, B., Papovich, C., Finkelstein, S. L., et al. 2015, ApJ, 799, 183
Salpeter, E. E. 1955, ApJ, 121, 161
Sanders, R. L., Shapley, A. E., Kriek, M., et al. 2015, arXiv:1509.03636
Santini, P., Ferguson, H. C., Fontana, A., et al. 2015, ApJ, 801, 97
Scoville, N., Faisst, A., Capak, P., et al. 2015, ApJ, 800, 108
Seibert, M., Martin, D. C., Heckman, T. M., et al. 2005, ApJL, 619, L55
Shapley, A. E., Reddy, N. A., Kriek, M., et al. 2015, ApJ, 801, 88
Shimakawa, R., Kodama, T., Steidel, C. C., et al. 2015, MNRAS, 451, 1284
Siana, B., Smail, I., Swinbank, A. M., et al. 2009, ApJ, 698, 1273
Sklias, P., Zamojski, M., Schaerer, D., et al. 2014, A&A, 561, A149
Smit, R., Bouwens, R. J., Labbé, I., et al. 2014, ApJ, 784, 58
Smith, D. J. B., & Hayward, C. C. 2015, MNRAS, 453, 1597
Song, M., Finkelstein, S. L., Ashby, M. L. N., et al. 2016, ApJ, 825, 5
Steidel, C. C., Rudie, G. C., Strom, A. L., et al. 2014, ApJ, 795, 165
Sutton, A. J., & Abrams, K. R. 2001, Statistical Methods in Medical Research, 10, 277
Tanaka, M. 2015, ApJ, 801, 20
Tilvi, V., Papovich, C., Tran, K.-V. H., et al. 2013, ApJ, 768, 56
Todini, P., & Ferrara, A. 2001, MNRAS, 325, 726
U, V., Hemmati, S., Darvish, B., et al. 2015, ApJ, 815, 57
Vanzella, E., Cristiani, S., Dickinson, M., et al. 2008, A&A, 478, 83
Ventura, P., Dell'Agli, F., Schneider, R., et al. 2014, MNRAS, 439, 977
Verhamme, A., Dubois, Y., Blaizot, J., et al. 2012, A&A, 546, A111
Walcher, J., Groves, B., Budavári, T., & Dale, D. 2011, Ap&SS, 331, 1
Wang, R., Carilli, C. L., Wagg, J., et al. 2008, ApJ, 687, 848
Wilkins, S. M., Bouwens, R. J., Oesch, P. A., et al. 2016, MNRAS, 455, 659
Williams, R. J., Quadri, R. F., Franx, M., van Dokkum, P., & Labbé, I. 2009, ApJ, 691, 1879
Windhorst, R. A., Cohen, S. H., Hathi, N. P., et al. 2011, ApJS, 193, 27
Witt, A. N., & Gordon, K. D. 2000, ApJ, 528, 799
Witt, A. N., Petersohn, J. K., Bohlin, R. C., et al. 1992, ApJL, 395, L5
Wuyts, S., Förster Schreiber, N. M., Lutz, D., et al. 2011a, ApJ, 738, 106
Wuyts, S., Förster Schreiber, N. M., van der Wel, A., et al. 2011b, ApJ, 742, 96
Wuyts, S., Labbé, I., Franx, M., et al. 2007, ApJ, 655, 51
Wuyts, S., Labbé, I., Schreiber, N. M. F., et al. 2008, ApJ, 682, 985
Xue, Y. Q., Luo, B., Brandt, W. N., et al. 2011, ApJS, 195, 10
Yajima, H., Li, Y., Zhu, Q., et al. 2012, ApJ, 754, 118
Zeimann, G. R., Ciardullo, R., Gronwall, C., et al. 2015, ApJ, 814, 162